Supplementary Information (SI) for Journal of Materials Chemistry A.
This journal is © The Royal Society of Chemistry 2024

Electronic supplementary information

Synergistic influence of multivalent Ru$^{\delta+}$ on CeO_x nanocatalyst for self-powered efficient electrochemical water splitting

Papri Mondal[†] **and Sujoy Baitalik**[*†]

[†]Department of Chemistry, Inorganic Chemistry Section, Jadavpur University, Kolkata 700032, India.

---

[*] To whom correspondence should be addressed: E-mail: sbaitalik@hotmail.com, sujoy.baitalik@jadavpuruniversity.in; Telephone Number: 91-033-2414-6666

S1. Experimental section

S1.1. Materials

All chemicals are of analytical grade and used as received without further purification. Ruthenium (III) nitrosyl nitrate [$Ru(NO)(NO_3)_3$], cerium nitrate hexahydrate [$Ce(NO_3)_3 \cdot 6H_2O$], NH_3, urea [$CO(NH_2)_2$], commercial Pt/C (20 wt% Pt), commercial ruthenium(IV) oxide (RuO_2), potassium hydroxide, ethanol, methanol, zinc acetate ($C_4H_6O_4Zn$), nickel foam (thickness: 1.6 mm, bulk density: 0.45 g cm^{-3}), 5 wt % Nafion solution (~5% in lower aliphatic alcohols and water, contains 15-20% water), LiOH, polyvinylidene fluoride (PVDF), and *N*-methyl-2-pyrrolidone are purchased from Sigma-Aldrich. The commercial carbon cloth (CC) is purchased from the fuel cell store. All water used throughout all the experiments is demineralized and ultrafiltered by a Millipore Milli-Q system (resistivity >18.2 MΩ/cm, TOC < 5 ppb).

S1.2. Synthesis of CeO_x (CO)

2.0 mmol of $Ce(NO_3)_3 \cdot 6H_2O$ is taken in a Teflon-lined autoclave containing 2.5 mL NH_3 and 40 mL H_2O and then this mixture is maintained at 100^0C for 6h followed by cooling naturally. After that, the product is collected through centrifugation-rinsing cycles with H_2O/EtOH and finally dried under vacuum. It is to be noted that hydrothermal treatment of $Ce(NO_3)_3 \cdot 6H_2O$ at ~100^0C leads to the formation of only ceria nanorods.[1-2]

S1.3. Synthesis of CeO_x/Ru^0 (CO/R^0)

The introduction of Ru^0 onto CO is performed through deposition-precipitation method using $Ru(NO)(NO_3)_3$ and urea. Initially, 400 μL of $Ru(NO)(NO_3)_3$ is taken in 50 mL of H_2O and kept for 30min under stirring condition. Then, 0.5 g of the preprepared CO and 1.3 g of urea are added into the solution (solution pH ~7.2) and further stirred for another 1h. After that, the suspension is heated up to 80°C and aged for 3h for allowing the R^0 nanoparticles (NPs) to adsorb onto the CO support. Next, the obtained product is centrifuged, washed repeatedly with H_2O/EtOH to remove excess urea, if any, and finally dried under vacuum.

S1.4. Synthesis of $CeO_x/Ru^0/RuO_x$ (CO/R^0/RO)

The freshly prepared CO/R^0 (0.5 g) NPs is thoroughly dispersed into 50 mL of H_2O through ultrasonic vibration for 30min under ambient temperature. After that, 400 μL of 10 mM aqueous solution of $Ru(NO)(NO_3)_3$ is added into the stirred suspension followed by adjusting the pH of the mixture to ~9 with 0.5 M NH_3. The resulting mixture is aged at 100°C for 4h under vigorous stirring, followed by vaporizing H_2O and eventually dried for overnight. Finally, the obtained compound is calcined in the programmable box furnace at 350°C under O_2 atmosphere (flow rate: 18 mL m^{-1}) for 5h with the heating rate of 1°C/m to obtain CO/R^0/RO. It is to be noted that metallic Ru don't get oxidized at room temperature in air, but transformed to RuO_2 when the temperature is raised above 600°C. The oxidation of Ru^0 starts at 400 °C and both Ru^0 and RuO_2 co-exist up to the temperature range of 500 °C.[3-4] Thus, the adopted strategy ensures the presence of both R^0 and RuO_2 in the resulting NComp.

S1.5. Synthesis of CeO_x/RuO_x (CO/RO)

The freshly prepared CO (0.5 g) NPs are completely dispersed into 50 mL of H_2O through ultrasonic vibration for 30min under ambient temperature. Then, 400 μL of 10 mM aqueous solution of $Ru(NO)(NO_3)_3$ is put into the continually stirred suspension followed by tuning the pH value of the solution with 0.5 M $NH_3{\cdot}H_2O$ solution to ~ 9. After that, the solution mixture is aged under stirring at 80 °C for 4h, followed by vaporizing H_2O at 100°C and then further drying overnight. Finally, the obtained compound is calcined in the programmable box furnace at 300°C for 5h under O_2 atmosphere to obtain CO/R^0/RO.

We have also synthesized Ru^0 (R^0), RuO_x (RO), and Ru^0/RuO_x (R^0/RO) (similar synthesis procedure as CO/R^0, CO/RO, and CO/R^0/RO formation, respectively except CO NPs addition).

S1.6. Instrumentations

The phase structure and crystallinity of the materials are examined through the Philips PW 1140 parallel beam X-ray diffractometer (XRD) using monochromatic Cu Kα radiation (λ = 1.540598 Å). The size, surface morphologies and internal structure are studied by field emission scanning electron microscopy (FESEM JEOL JSM 7100F) equipped with an energy dispersive X-ray spectroscopy (EDX) and transmission electron microscopy (TEM-JEOL JEM-2100) with a 200 kV accelerating voltage. The selected area electron diffraction (SAED) pattern is also utilized for determination of the material composition. The XPS measurements are performed with a Kratos AXIS Ultra DLD X-ray photoelectron spectrometer (Kratos Analytical, Manchester, UK) using monochromatic Al Kα radiation (hν =1486.6 eV) with 0° take of angle (normal to analyzer) and a six-channel detector for measurement of photoelectrons. Charge compensation is utilized during measurement. The vacuum pressure in the analyzing chamber is maintained at $\sim 2 \times 10^{-9}$ torr during the acquisition process. The XPS binding energy is calibrated against the C 1s peak at 284.8 eV of adventitious carbon. Data analyses are done using Kratos Vision (Kratos Analytical Ltd.) processing software and CasaXPS (Casa Software Ltd.). XPS interpretation is based on literature values.

X-ray absorption near-edge structure (XANES) and extended X-ray absorption fine structural (EXAFS) measurements are conducted to realize the valence states as well as the local coordination environments around Ce and Ru atoms in the materials at the 1W1B beamline of the Beijing Synchrotron Radiation Facility (BSRF). The Ce and Ru K-edge spectra of the catalysts and the reference samples are measured in transmission mode using an ionization chamber at room temperature. Si (111) double-crystal monochromator is used for the purpose. The EXAFS region is plotted as a wave vector, known as k-space. In these spectra, the energy is converted to a photoelectron wavenumber. The k-space is converted to pseudo radial (R-space) spectrum through Fourier transform. Each peak in the R-space spectrum corresponds to a single scattering path length. The exact path lengths can be established via fitting the peaks to a model compound. Herein, the EXAFS functions are Fourier transformed to R space with k^3-weight. The data are processed and fitted using Athena and Artemis modules[5] in the IFEFFIT XAS analysis software packages.[6] For EXAFS modelling, EXAFS of the RuO_2 is fitted, and the obtained amplitude reduction factor (S_0^2) value of 0.790 is set to determine the coordination numbers (CNs) in the Ru-O scattering path. The existence of the mixed oxidation states in Ce is assessed by using a linear combination fit (LCF) method of Ce L_3 XANES spectra. The Ce L_3-edge XANES data are recorded herein in a fluorescence mode. $CeCl_3$ and CeO_2 are used as the references for this purpose. The storage ring works at 2.5 GeV with an average electron current of 250 mA. Herein, Ce L_3 XANES spectra of CO/R^0/RO are linearly fitted with $CeCl_3$ and CeO_2

standards via least-squares fitting. LCF of the XANES spectra are performed using Athena software from the IFEFFIT program package.

The Barrett-Emmett-Teller (BET) surface area is calculated from the nitrogen sorption measurement by ASAP 2010 surface area analyzer and the pore-size distribution is investigated in accordance to the Barrett-Joyner-Halenda (BJH) model. The inductive coupled plasma spectrometry (ICP) (Perkin Elmer, Optima 2000) is used to evaluate the concentration of trace amount of impurities in KOH electrolyte.

S2. Result and discussion

S2.1 Determination of pH Point of Zero Charge (pH_{pzc})

The pH_{pzc} of CO is determined by following the pH drift method. We have taken 250 mL conical flasks (9 in numbers) and 50 mL of NaCl (0.01 M) solution is added to each of them. We are interested to make the solution with pH range between 1 and 9 within the interval of pH = 1. We then adjusted the pH of the solution by adding requisite amount of 0.01 N of NaOH and HCl solutions. After attaining the required pH values, 0.01 g of CO is added into each conical flask and capped them immediately and thoroughly shaken for 12 h in a mechanical shaker. Then the solutions were filtered and measured their final pH. The point at which the curve of ΔpH ($pH_{initial}$–pH_{final}) intersected the $pH_{initial}$ axis is considered as determinant of the pH_{pzc} value which is found to be 6.7.

S2.2. XRD and XAS analysis

X-ray diffraction (XRD) technique is initially used to study the effect of Ce/O, and Ru/O ratio on the crystalline phase and composition where Fig. 1a (main manuscript) confirms the successful formation and fabrication CeO_2. The XRD pattern of Ce/O (Fig. 1ai, main manuscript) displays four highly intense peaks at 28.5°, 33.1°, 47.4°, and 56.3° corresponding to the (111), (200), (220), and (311) facets of *fcc* lattice of CeO_2 (JCPDS No.: 81-0792) and analogous structure is displayed in Fig. S3a (ESI†). As shown in Fig. 1aii (main manuscript), except for the peaks indexed to CeO_2, four sharp peaks at 38.3°, 42.2°, 44.0°, and 58.3° (marked by sky asterisks) are observed which can be well attributed to the (100), (002), (101), and (102) facet, respectively for metallic Ru (JCPDS No.: 06-0663) thereby indicating the formation of R^0 fabricated CeO_2 (Fig. S3b, ESI†). When Ru is further introduced for RuO_x (RO) loading, the observed new XRD peaks [marked by pink asterisks, Fig. 1aiii (main manuscript)] are well indexed to the primitive tetragonal RuO_2 [(Fig. S1 and S3c, ESI†), JCPDS No.: 71-2273], revealing good crystallization and effectual fabrication with RuO_2. Moreover, the incremental introduction of Ru leads to decrease of XRD signal intensities which imply their low crystallinity. For the sake of comparative study, we have also prepared CO/RO and its successful formation is confirmed by XRD analysis (Fig. S2, ESI†).

X-Ray absorption spectroscopic (XAS) measurement is conducted to investigate the atomic coordination environment as well as the electronic structure of CO/R^0/RO NComp. Closely similarity in the Ru K-edge XAFS spectra of CO/R^0 and R^0 powder and presence of a single peak at ~2.47 Å (Ru-Ru) in CO/R^0 clearly indicates that all the ruthenium in CO/R^0 is in their completely reduced form (Ru^0). Upon RO loading over CO, the radial distribution pattern in CO/RO [Fig. i(iii), main manuscript] shows three distinguished peaks at 1.53, 2.82, and 3.18 Å arising out of Ru-O, Ru-Ru (second shell), and Ru-Ru (third shell) interaction, respectively which are also in close resemblance with that of RuO_2 reference [Fig. i(v), main manuscript]. Moreover, there is an additional absorption edge position at ~2.33 Å, arising out of Ru-O interaction and has a positive shift relative to RuO_2 which is indicative of the presence of lower valence state of Ru in CO/RO than that in RuO_2. Thus, the outcomes of XAS clearly indicates probable formation of some Ru^{III}-O type species which is also in accordance with the XPS result wherein the formation of RuO_x ($x \leq 2$) over CO is followed by a modest variation in the length of the Ru-O bond. Finally, the XAFS spectrum of CO/R^0/RO [Fig. i(iv), main manuscript] possesses characteristics of both R^0 and RO, indicating its successful fabrication.

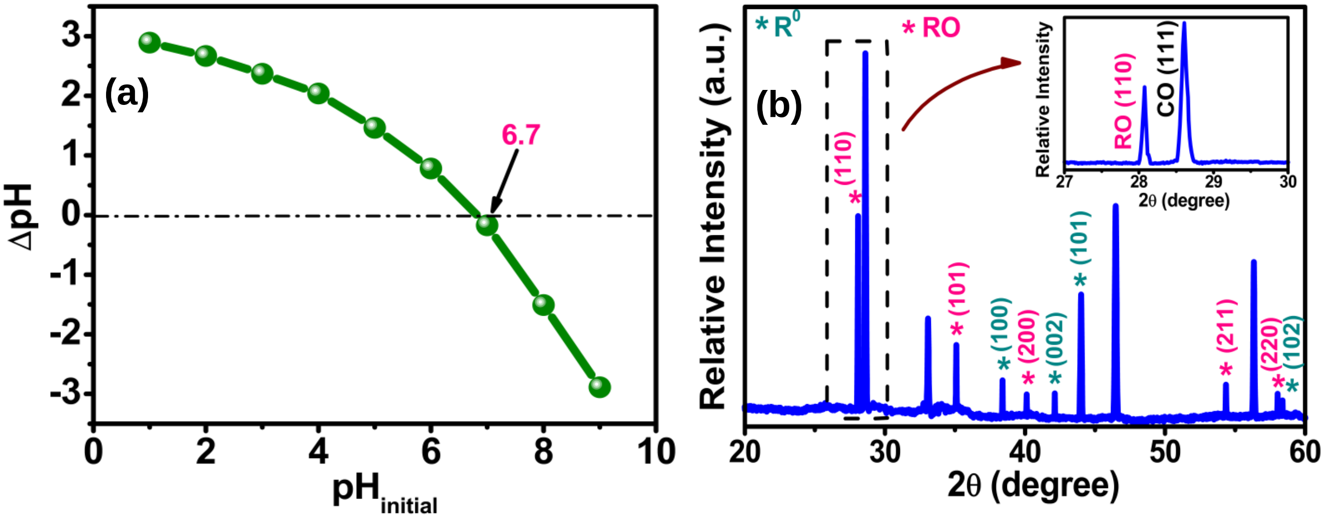

Fig. S1 (a) pH$_{pzc}$ of the CO and (b) XRD measurement of CO/R^0/RO (inset: under magnification).

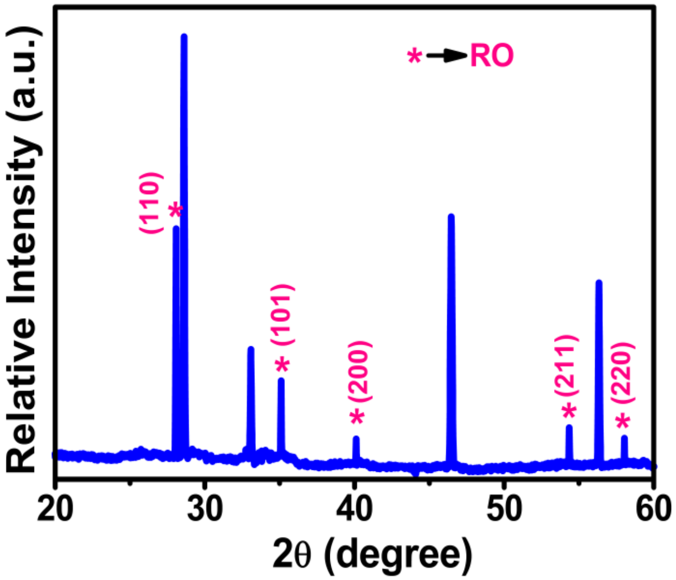

Fig. S2 XRD measurement of CO/RO.

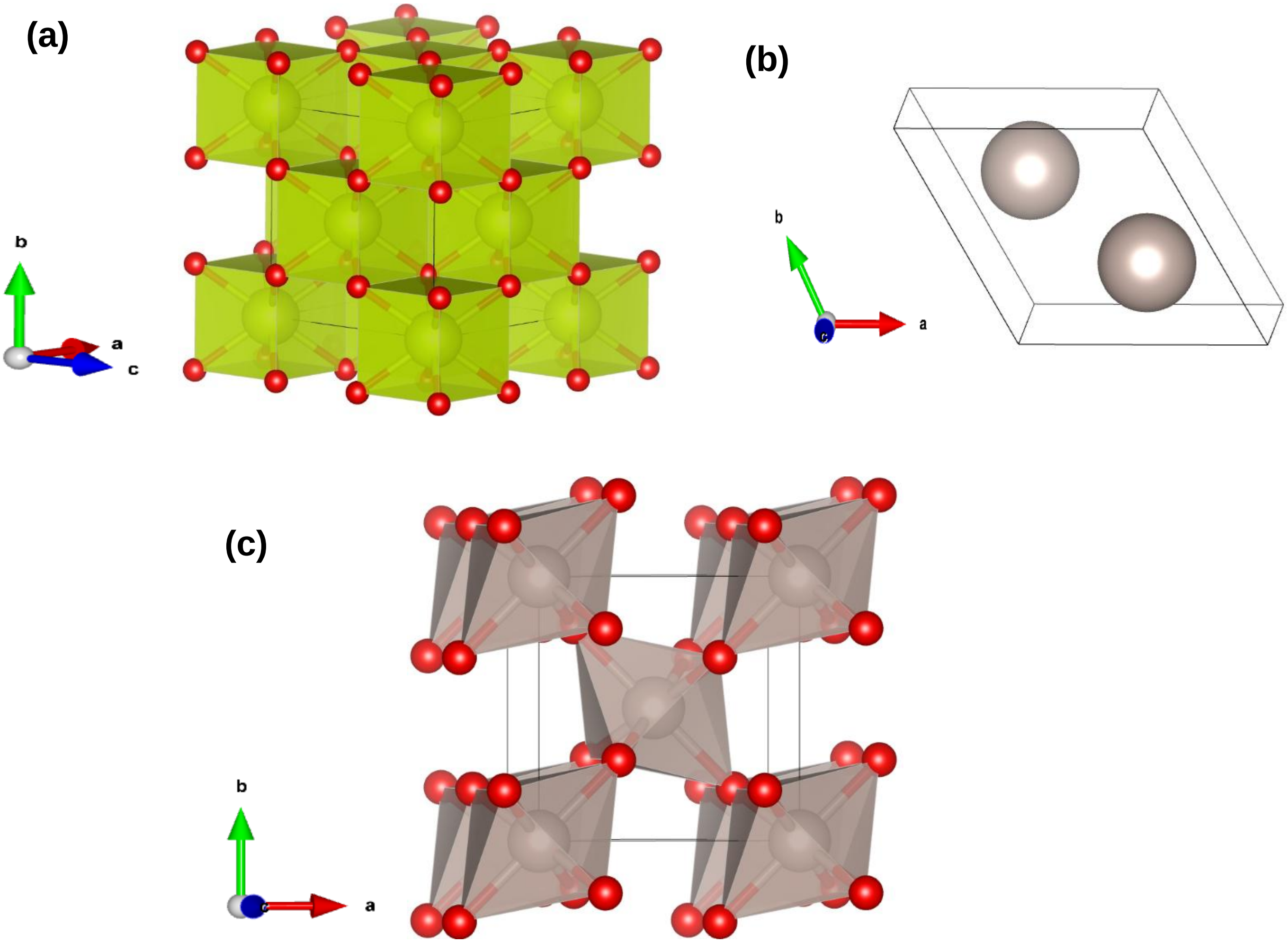

Fig. S3 The crystal structure of (a) CeO_2 [Ce (green), and O (red)], (b) R^0 [Ru (grey)], and (c) RuO_2 [Ru (grey), O (red)].

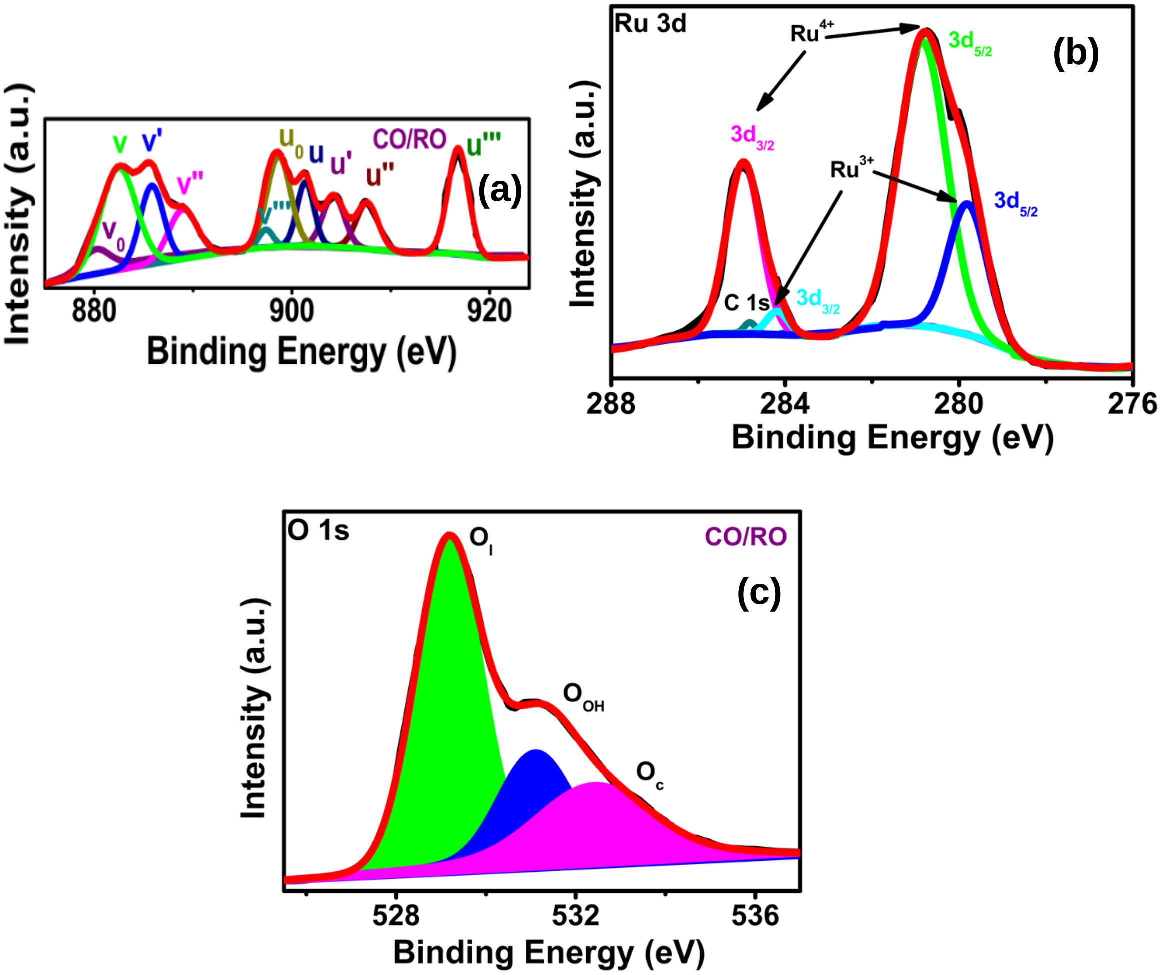

Fig. S4 XPS spectra of (a) Ce 3d, (b) Ru 3d, and (c) O 1s of CO/RO.

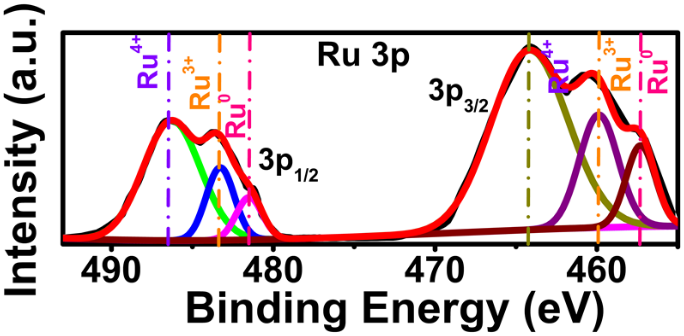

Fig. S5 Ru 3p XPS spectra of CO/R^{0}/RO.

Table S1 Binding energy of Ce 3d.

	Ce $3d_{5/2}$					Ce $3d_{3/2}$				
	v_o Ce^{3+}	v Ce^{4+}	v′ Ce^{3+}	v′′ Ce^{4+}	v′′′ Ce^{4+}	u_o Ce^{3+}	u Ce^{4+}	u′ Ce^{3+}	u′′ Ce^{4+}	u′′′ Ce^{4+}
CO/R^0/RO	879.9	881.8	885.2	888.4	896.9	897.7	900.9	903.7	907.0	916.4

Table S2 The relative content of the surface-active oxygen (Oa).

Materials	O_l	O_{OH}	Oc	$O_a = (O_{OH} + O_c)$	$[O_a/(O_a + O_l)]$	$[O_a/(O_a + O_l)]$ %
CO/R^0	67.16478	25.77417	7.06105	32.83522	0.3283522	32.84
CO/RO	58.11889	20.54991	21.33121	41.88112	0.4188112	41.88
CO/R^0/RO	53.37759	34.2491	12.37331	46.62241	0.4662241	46.62

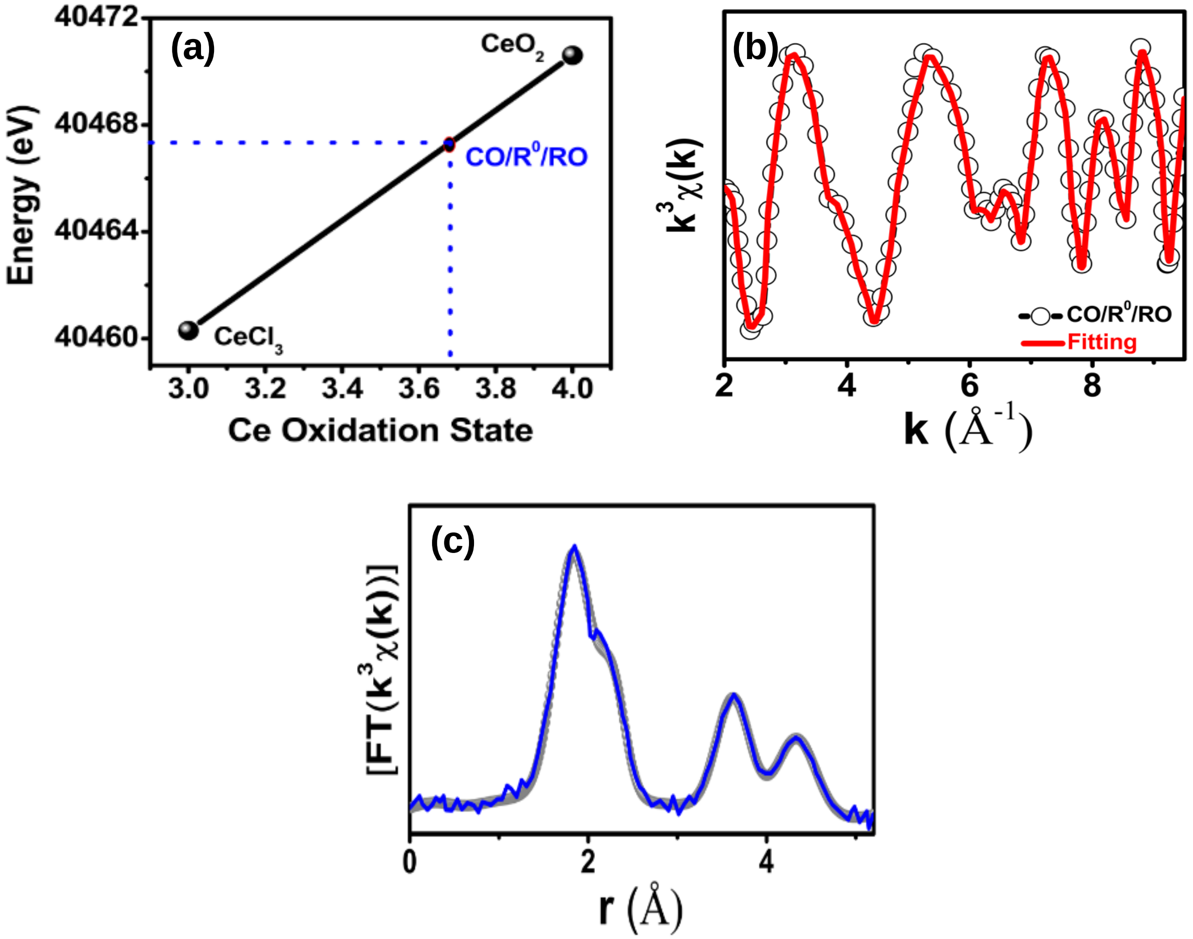

Fig. S6 (a) The function between adsorption energy and Ru oxidation state, (b) k^3-weighted Ce K-edge EXAFS oscillations for CO/R^0/RO in k space, and (c) FT Ce K-edge EXAFS fitting curve of CO/R^0/RO.

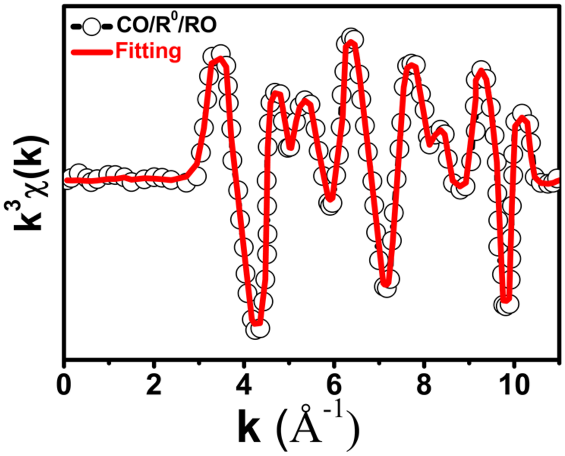

Fig. S7 The k^3-weighted Ru k-edge EXAFS oscillations for CO/R^0/RO in k space.

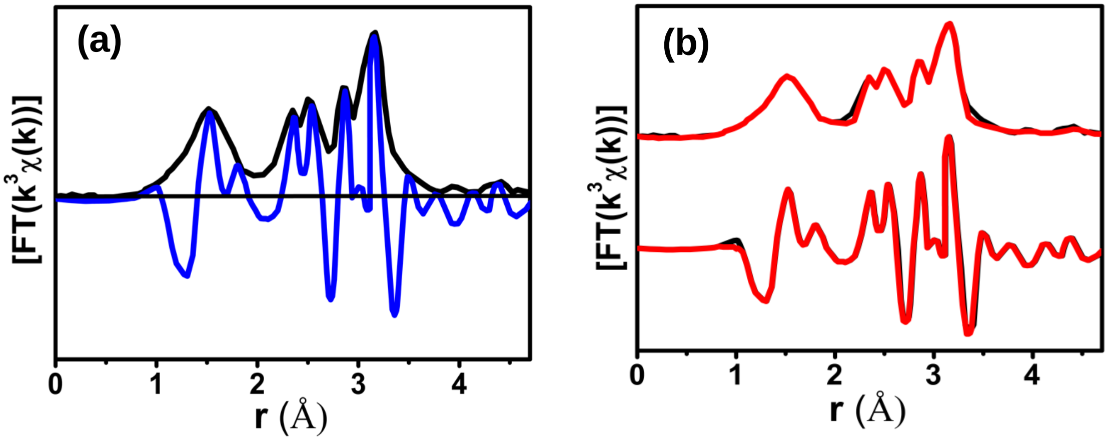

Fig. S8 (a) Magnitude (black) and imaginary (blue) part of EXAFS Fourier transformed results of CO/R^0/RO in R space, and (b) corresponding fitting spectra (red) (the upper part represents the magnitude part, whereas the lower part is the imaginary part).

Table S3 EXAFS curve fitting result of Ce K-edge of CO/R^0/RO.#

Sample	Shell	R (Å)	CN	σ^2 (10^{-3} Å^2)	R-factor
CO/R^0/RO	Ce-O	2.384±0.02	7.8±0.1	7.6±1.4	0.0110
	Ce-Ce	3.830±0.02	9.9±0.2	6.5±1.3	
	Ce-O$_1$	4.441±0.02	16.6±0.1	8.7±1.1	

#R corresponds to interatomic distance; CN corresponds coordination number; σ^2 represents Debye-Waller factor (a measure of thermal and static disorder in absorber-scatterer distances); R factor is a measure of the goodness of the fitting.

Table S4 EXAFS curve fitting result of Ru K-edge of CO/R^0/RO.

Sample	Shell	R (Å)	CN	σ^2 (10^{-3} Å^2)	R-factor
Commercial RuO$_2$	Ru-O (1)	1.94±0.01	2*	1.2±1.5	0.01531
	Ru-O (2)	1.99±0.01	4*	1.2±1.5	
CO/R^0/RO	Ru-O	1.99±0.01	5.5±0.2	5.2±1.3	0.00812

*Coordination number of commercial RuO$_2$ reference sample is fixed to obtain S_0^2 value.

S2.3. Morphological analysis

The high-resolution TEM (HRTEM) in Fig. S10a (ESI†) indicates the clear fringes with lattice spacing of 0.313 nm that can be well indexed to the (111) plane of cubic CO (JCPDS No.: 81-0792). Additionally, Fig. S10b (ESI†), shows two sets of lattice fringes with interplanar spacing of 0.311 and 0.238 nm which corresponds to the standard cubic CO (111) and R^0 (100) crystallographic planes, signifying the high purity and crystallinity of CO/R^0. Moreover, in Fig. S10c (ESI†), an additional new plane of RO (200) is identified along with two CO (200) and R^0 (100) planes which confirms the successful fabrication of CO/R^0/RO NComp. Additionally, the developed interface is also clearly found from Fig. S11 (ESI†) where the presence of three interplaner spacing of 0.311, 0.214, and 0.224 nm confirm the existence of CO, R^0, and RO, respectively in CO/R^0/RO. Fig. S10d (ESI†) shows spherical like morphology of RO.

Moreover, the crystal information of CO, CO/R^0, and CO/R^0/RO is verified by the selected area electronic diffraction (SAED) patterns where Fig. S12a (ESI†) displays concentric rings formed by bright discrete diffraction spots, which are in good agreement with the (220), (200), and (111) planes of CO, in consistent with the XRD analysis. Fig. S12b (ESI†) obviously possesses another new distinct ring which signifies the (101) plane of R^0 along with (111) and (220) planes of CO, confirming the formation of CO/R^0. In addition, SAED pattern in Fig. S12c (ESI†) can be recognized by the presence of two new (110) and (101) planes of primitive RO along with (200), (311) planes of CO and (101) plane of R^0 which validates the formation of CO/R^0/RO, again supported by XRD. Thus, the analogous SAED patterns further ensure the effective fabrication of the materials where each catalyst continues the cubic CO phase after NComp formation.

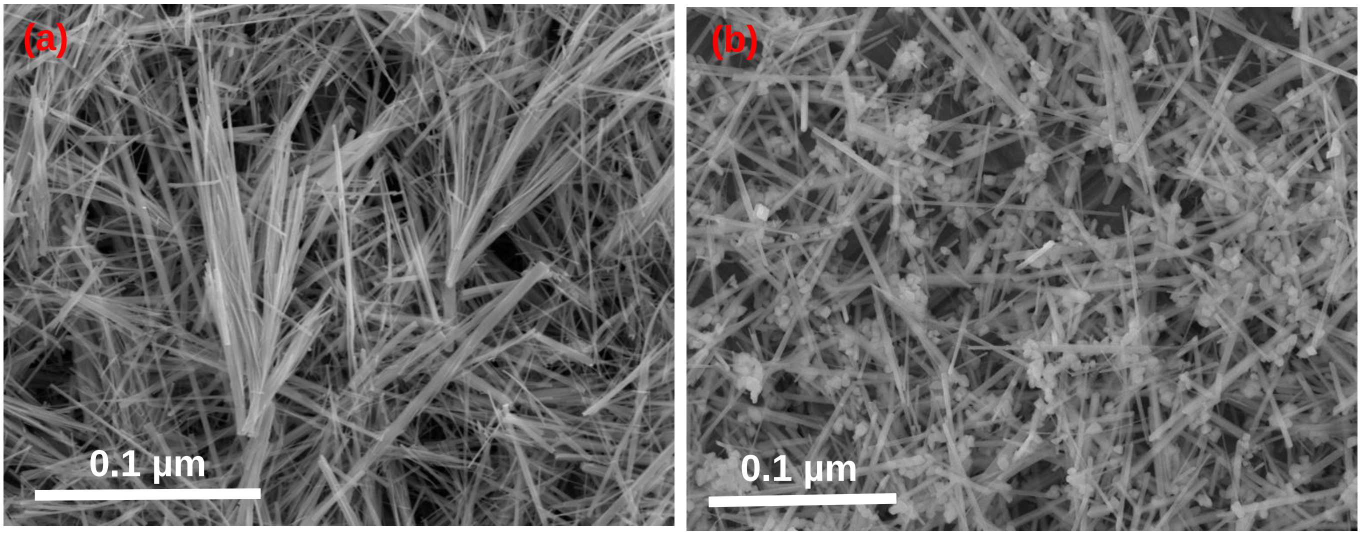

Fig. S9 FESEM images of (a) CO, and (b) CO/R^0/RO, respectively.

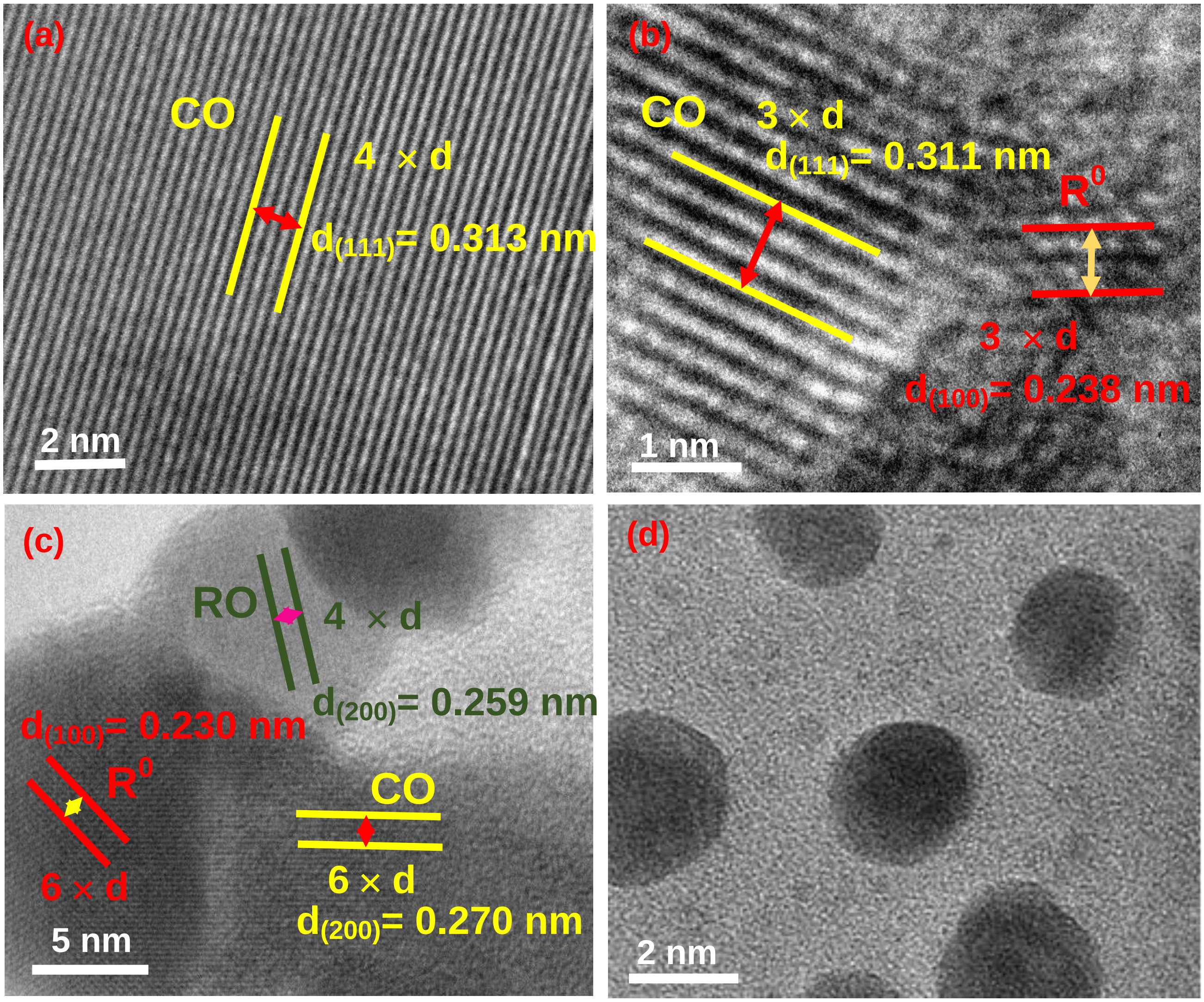

Fig. S10 (a-c) Fringe patterns of CO, CO/R^0, and CO/R^0/RO, respectively, and (d) TEM image of RO nanoparticles.

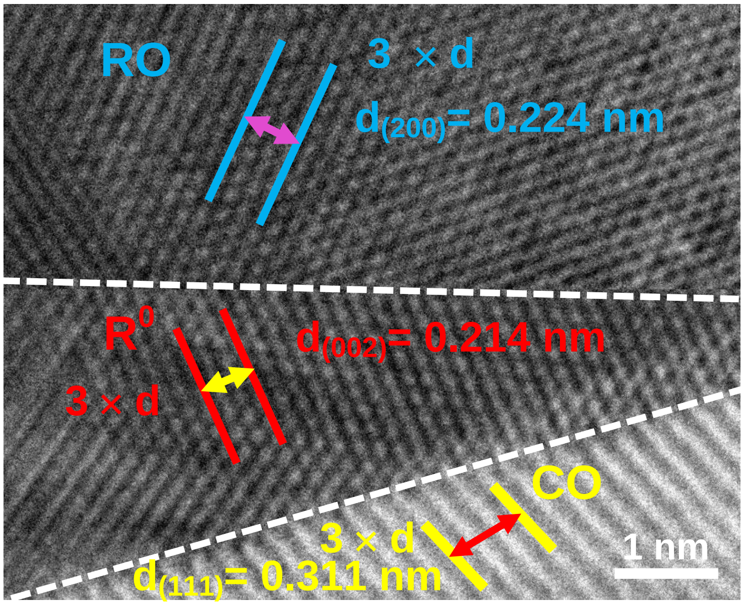

Fig. S11 Fringe patterns of CO/R^0/RO showing interface.

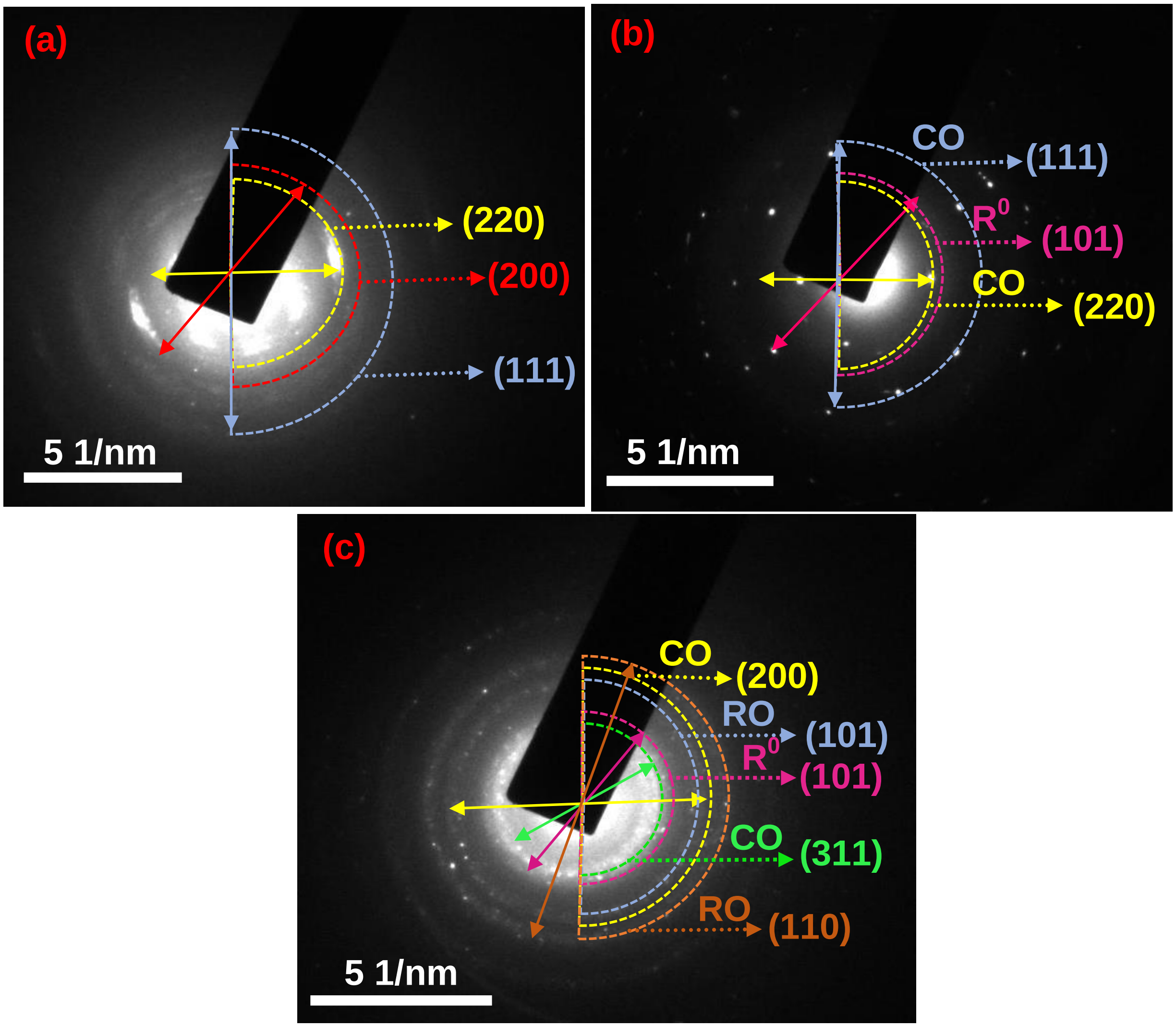

Fig. S12 SAED patterns of (a) CO, (b) CO/R^0, and (c) CO/R^0/RO.

S2.4. Energy-dispersive X-ray (EDX) analysis

To better understand the elemental distribution of Ce and Ru in all materials, the EDX analysis is also investigated. In Fig. S13(a-d) (ESI†), the EDX spectrum shows the homogeneous distribution of elements (Ce, O in CO and Ce, Ru, O in CO/R^0, CO/RO, and CO/R^0/RO) (Table S5, SI), which strongly indicates that CO as the key component in the composites.

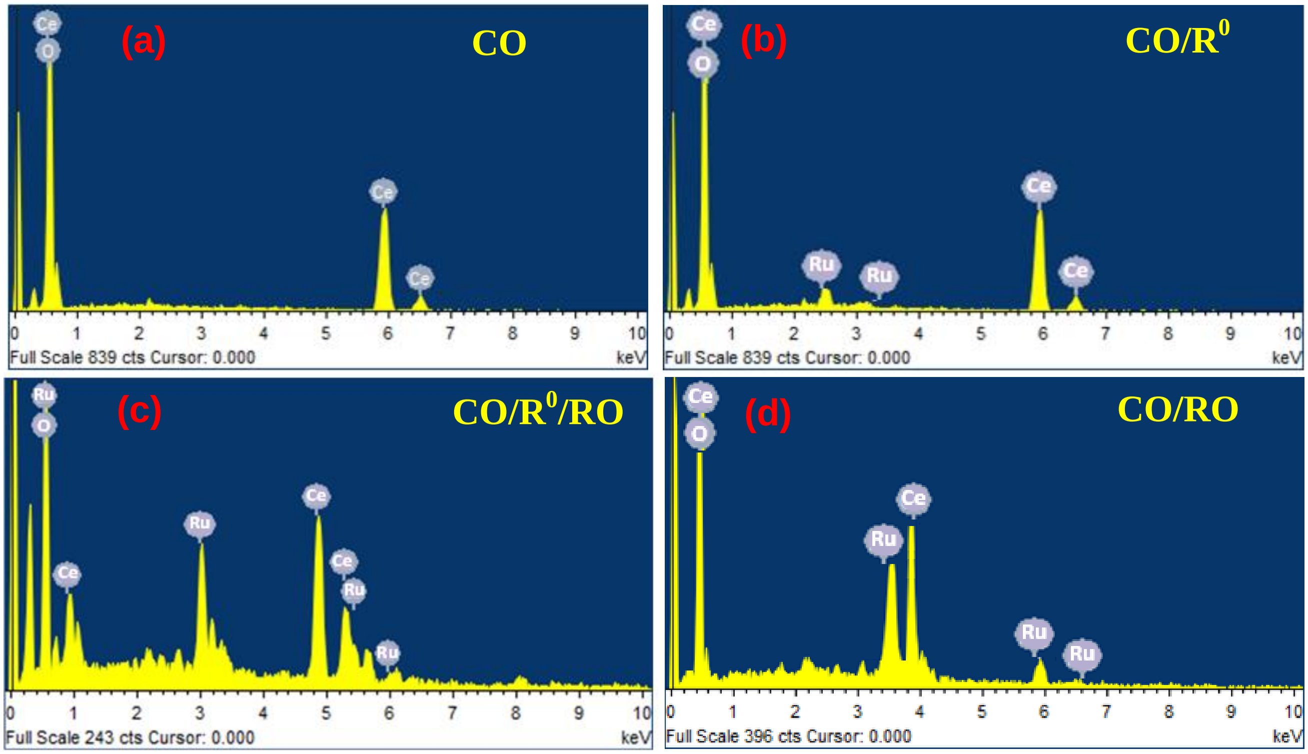

Fig. S13 (a)-(d) EDX results of CO, CO/R^0, CO/R^0/RO, and CO/RO, respectively.

Table S5 EDX results of the materials.

	Atomic%			
Element	CO	CO/R^0	CO/R^0/RO	CO/RO
O	66.64	66.48	66.40	66.50
Ce	33.36	33.24	33.16	33.21
Ru	—	0.28	0.44	0.29
Total	100.00	100.00	100.00	100.00

S2.5. Electrochemical measurements

All the electrochemical tests are carried out on a CHI760E electrochemical workstation (CH Instruments, USA) with a rotating ring disk electrode (RRDE) using a standard three electrode cell configuration at room temperature. The electrocatalysts (ECs) fabricated RRDE (disk diameter 3 mm), a graphite rod (length 150 mm, diameter 3 mm, 99.995% trace metals basis, purchased from Sigma-Aldrich), and Ag/AgCl electrode (with saturated KCl solution) are used as working, counter, and reference electrodes, respectively. Furthermore, all measured potentials are converted into the reversible hydrogen electrode (RHE) scale according to the equation $E_{RHE} = E_{Ag/AgCl} + 0.197\ V + 0.059\times pH$. Moreover, before the ORR/OER test, the electrolyte is purged with high-purity O_2 over 40 min to form the O_2 saturated KOH solution while KOH solution is purged with high-purity N_2 over 40min before HER. The electrochemical ORR and HER performances are carried out in purified 0.1 M and 1.0 M aqueous KOH solution, respectively while OER measurement is performed in both 0.1 M and 1.0 M KOH solution under a rotation rate 1600 rpm.

S2.5.1. Electrode preparation

First, the RRDE is sequentially polished with 0.5 and 0.05 μm alumina powder which is then cleaned with H_2O under vigorous sonication for 30min and finally dried under N_2 flow at room temperature. For ORR, OER and HER, the working electrode is developed as follows: ~ 2 mg of EC is ultrasonically dispersed well into the mixture of 1 mL of H_2O and 40 μL of nafion (0.5 %) for 40 min for formation of a homogeneous ink. Subsequently, 4 μL of the above EC ink is drop-casted on the pre-polished glassy carbon disk surface of RRDE resulting in the EC loading of 0.11 $mg.cm^{-2}$. Finally, the prepared electrode is air-dried for 4h at room temperature for all electrochemical measurements. For comparison, Pt/C (for ORR and HER) and RuO_2 (for OER) electrodes with similar mass loading are prepared by the same method using commercial Pt/C and RuO_2, respectively. We have used a non-glass-based cell which is made of fluorinated ethylene propylene (FEP) to avoid the interference of impurities from the glass cell in alkaline electrolyte because during electrochemical reaction, the leaching of glass from glass cell may affect on the catalytic activity of EC. In addition, prior to starting all measurements, the cell and all glassware are thoroughly cleaned through storing overnight in concentrated H_2SO_4 to eliminate all metals and organic contaminants. Then, all are boiled and washed several times with H_2O to make sure the cleanness of the system.

S2.6. Measurements of ORR

The ORR activities of the synthesized catalysts are measured by using linear sweep voltammograms (LSVs) with different rotational speed (400 to 2000 rpm) at a scan rate of 5 mV s^{-1}. The chronoamperometric measurements are carried out to investigate the durability and MeOH tolerance of the catalysts. For the MeOH crossover study, 3.0 M MeOH (20 volume %) is added into O_2-saturated 0.1 M KOH solution after ~2000s. All obtained data is corrected by iR compensation. The number (n) of electron transfer at the electrode potentials of 0.20-0.70 V are obtained from the Koutecky-Levich (K-L) plots by the following equation.

$$\frac{1}{j} = \frac{1}{j_K} + \frac{1}{j_L} = \frac{1}{j_K} + \frac{1}{\mathrm{B}\omega^{1/2}} \qquad \textbf{(S1)}$$

Where j, j_K, and j_L are the measured current density, kinetic current density, and diffusion-limited current density ($mA.cm^{-2}$), respectively and ω is the electrode rotating speed in rpm. Here, B stands for the Levich slope that is given by,

$$\mathrm{B} = 0.62\mathrm{nFC_0}(\mathrm{D_0})^{2/3}(\nu)^{-1/6} \qquad \textbf{(S2)}$$

Where n is the electron transfer number per oxygen molecule, F (Faraday constant) = 96,485 $C.mol^{-1}$, C_0 (the bulk concentration of O_2 in 0.1 M KOH solution) = 1.2×10^{-6} $mol.cm^{-3}$, D_0 (the diffusion coefficient of O_2 in 0.1 M KOH) = $1.90 \times 10^{-5} cm^2.s^{-1}$ and ν (the kinematic viscosity in 0.1 M KOH) = 0.01 $cm^2.s^{-1}$. The number of electron transfer (n) is obtained from the slope of the linear plot of j^{-1} vs. $\omega^{-1/2}$. Tafel plots [E vs. log (j_k)] are collected from the LSV curves at 1600 rpm.

For the RRDE measurement, catalyst inks and electrodes are prepared following the same procedure as for that RDE. The n value and percentage of HO_2^- yield can be determined quantitatively at a rotation speed of 1600 rpm based on the ring and disk currents by applying a constant ring potential of 1.5 V_{RHE} according to the followed equations.

$$\mathbf{n} = \frac{4I_d}{I_d + \frac{I_r}{N}} \tag{S3}$$

$$\mathbf{HO_2}^{-}\% = \frac{2 \times \frac{I_r}{N}}{I_d + \frac{I_r}{N}} \times 100\% \tag{S4}$$

Where I_r and I_d are the ring and disk currents ($mA.cm^{-2}$), respectively and *N* is the current collection efficiency (0.43) of the ring.

S2.7. Measurements of OER

Before measuring the polarization curves, first the EC loaded working electrodes are repeatedly scanned through cyclic voltametric (CV) measurements until a static CV plot could be reached. Subsequently after the performance reached a steady state, the OER activity is evaluated by LSV in the potential window ranging from 0.6 to 1.9 V_{RHE} with a scan rate of 5 mV s^{-1}. The current densities are normalized to the geometric immersed surface area of the electrode 0.071 cm^2. EIS is conducted at a constant η of 120 mV under the sweeping frequency from 5 mHz to 100 kHz with an AC voltage of 5 mV. The impedance data are fit to a simplified Randles cell model to analyze the charge transfer resistance (R_{ct}) and double layer capacitance (C_{dl}). All data are corrected by iR-compensation to minimize the conductivity impact on OER catalytic performance. The η at 10 $mA.cm^{-2}$ (η_{10}) was calculated as follows:

$$\eta_{10} = \mathrm{E}_{10} - 1.23 \tag{S5}$$

Here, E_{10} is OER polarization potential at current density of 10 $mA.cm^{-2}$ and the value 1.23 suggests the O_2/H_2O equilibrium potential.

The Tafel slope is derived according to the Tafel equation as follows:

$$\eta = \mathbf{a} + \mathbf{b} \log \mathbf{j} \tag{S6}$$

Where η is the overpotential, b is the Tafel slope, and j is the current density.

The durability of the ECs is investigated by both LSV and chronopotentiometric response. The chronopotentiometric measurements are carried out at a constant current density of 10 mA.cm^{-2}.

S2.8. Measurements of HER

The HER polarization curve (LSV) is measured under potential range from −1.0 to 0.0 V at a scanning rate of 5 mV s^{-1}. The EIS measurements are carried out at a constant η of 60 mV. Tafel analyses and stability tests are as similar as for OER tests. The chronopotentiometric response is carried out at constant current density of 10 mA.cm^{-2}. All the polarization curves are corrected by iR compensation.

S2.9. Fabrication and evaluation of Zinc-Air battery (ZAB)

The ZAB is fabricated by a home-built setup where a pre-polished zinc plate is used as anode and EC loaded on CC is used as air cathode. An aqueous 6.0 M KOH solution containing 0.2 M $Zn(Ac)_2$ is used as electrolyte. In order to maintain reversible zinc electrochemical reactions at the anode, $Zn(Ac)_2$ is added to KOH solution. The air electrode is fabricated via dropping the homogeneous EC ink onto CC (0.5 cm × 0.5 cm) with a mass loading of ~0.2 mg.cm^{-2} and dried overnight. For comparison, commercial catalysts coated on the CC with same mass loading are also used as an air electrode. All tests of ZAB are performed under ambient atmosphere. Polarization plot is obtained through LSV (charging/discharging) measurement at a scan rate of 5 mV.s^{-1} with CHI760E electrochemical workstation (CH Instrument) and the galvanostatic discharge-charge cycling (5 min discharge and then 5 min charge and that cycle repeated) are measured at the current density of 1 mA.cm^{-2}. The power density (P) of the ZAB is calculated as follows:

$$P = IV \tag{S7}$$

Where, I is the discharge current density and V is the corresponding voltage.

Working principle of ZAB

In an alkaline ZAB, the metallic Zn is oxidized to Zn^{2+} at the anode during the discharge process and then the resulting Zn^{2+} further reacts with the OH^{-} diffused from the cathode to form zincate ions $Zn(OH)_4^{2-}$. Finally, $Zn(OH)_4^{2-}$ decomposes to form solid ZnO at anode. The generated electrons go through the electric circuit and supply electric energy to different electric devices. At the same time, O_2 accepts the electrons generated from Zn oxidation at anode and reduced to OH^{-} on the porous surface of the EC layer at cathode (ORR). The reactions during discharge process can be illustrated as:

Anode:

$$Zn \rightarrow Zn^{2+} + 2e^{-} \tag{S8}$$

$$Zn^{2+} + 4OH^{-} \rightarrow Zn(OH)_4^{2-} + 2e^{-} \tag{S9}$$

$$Zn(OH)_4^{2-} \rightarrow ZnO + H_2O + 2OH^{-} \tag{S10}$$

Cathode:

$$O_2 + 2H_2O + 4e^{-} \rightarrow 4OH^{-} \tag{S11}$$

Overall reaction:

$$2Zn + O_2 \rightarrow 2ZnO \tag{S12}$$

For a rechargeable ZAB (RZAB), a charge process is also involved which is satisfied by reversing the above reactions. During charging, O_2 is produced from the reoxidation of OH^{-} at cathode (OER) and metallic Zn is plated at the anode.

S2.10. Li-air battery (LAB)

The galvanostatic cycling test for the battery is performed at a battery cycler (Land, China). The protected Li anode is prepared following the previously reported method.[7] A piece of metallic Li (diameter ~15 mm, thickness ~0.5 mm) is attached to a copper foil, and the other side of Li is coated with a home-made gel polymer electrolyte (GPE, Li conductivity ~0.2 mS.cm^{-2} at 25 °C) and a piece of LiSICON (Ohara Inc., Japan). The LiSICON film has a dense structure and a high Li ionic conductivity of 0.1 mS.cm^{-2} at 25 °C, which allows Li^{+} to pass through but prevents water from penetrating the coating layer. The cathodic aqueous solution comprised of 0.1 M LiOH saturated O_2. LAB with CO/R^0/RO as the cathode catalysts, is fabricated with the following steps: first, CO/R^0/RO catalyst, Super P carbon, and polyvinylidene fluoride (PVDF) (binder) are mixed with the ratio of 4:4:2. Then *N*-methyl-2-pyrrolidone (NMP) is added to form the cathode catalyst slurry. The slurry is dispersed on the carbon paper with loading ~0.15 mg.cm^{-2} and dried at 120 °C under vacuum atmosphere for at least 12 h to remove the residual solvent; after which air cathode is prepared.

Working principle of LAB

A typical LAB is constructed using CO/R^0/RO NComp electrode as a cathode and a metallic Li anode protected by a Li conductive membrane (LiSICON, Ohara Inc., Japan).[8-9] The reactions on discharge are:

Li anode:
$$\mathrm{Li - e^{-} \rightarrow Li^{+}} \tag{S13}$$

Air cathode:
$$\mathrm{O_2 + 2H_2O + Li + 4e^{-} \xrightarrow{CO/R^0/RO} 4LiOH} \tag{S14}$$

On charge, the reactions are reversed. Li^{+} is reduced to Li metal and LiOH is oxidized to O_2, releasing into the air.

S2.11. Overall water splitting (OWS) performances

The OWS test is carried out in a two-electrode system where CO/R^0/RO NComp coated on Ni foam is used as symmetric bifunctional (BF) EC for both the anode and cathode materials with the mass loading of 0.10 mg.cm^{-2}. Additionally, the benchmark Pt/C (cathode)‖RuO$_2$/C (anode) couple is configured as a reference under the same conditions. Before testing, the KOH solution is purged with N$_2$ for at least 40 min. The polarization curves are achieved from LSV measurements between 1.2 and 1.8 V with a scan rate 5 mV.s^{-1} in 1.0 M KOH.

S2.12. Controlled potential electrolysis (CPE)

CPE experiments are performed on a CHI-700E electrochemical workstation by a three-electrode system in which graphite electrode (surface area of 2 cm^2) is used as working electrode, a graphite rod is the counter electrode, and Ag/AgCl electrode is the reference electrode. After the electrolysis, the O$_2$ and H$_2$ evolved in the head space of the reaction cell are distinguished by GC-TCD chromatography. Due to their similar thermal conductivities, the sensibility of the GC-TCD for H$_2$ using helium as a carrier gas is very low.

S3. Calculation of different parameters

The calculation of electrochemical active surface area (ECSA) is shown in the following equation[10-13]:

$$\mathbf{ECSA} = \frac{\mathbf{C_{dl}}}{\mathbf{C_s}} \tag{S15}$$

Where, C_{dl} is the double-layer capacitance and C_s is the ideal specific capacitance of a smooth planar surface made of the similar material per unit area under identical electrolyte conditions. Herein, we have used the general specific capacitances of $C_s = 0.04$ mF.cm^{-2} for 1 M KOH solution.

Generally, C_S can be determined via capacitance measurement of a well-known area of a smooth and planar electrode surface measured under the same experimental conditions. Unfortunately, it is very tough to determine experimentally because most electrode display substantial roughness and a range of surface orientations. McCrory et al.[12] reported that the C_S values for different ECs vary between 0.022 and 0.130 mF.cm^{-2} in alkaline solutions indicating that the C_S value possesses enormous differences for various materials. The C_S value should be an experimentally measured capacitance value of a flat EC surface and thus, it has the similar determination problems as other capacitance value. Numerous factors influence the accuracy of this method as the p^H, the used potential etc. Hence, the determination of an exact standard value for ECs is very difficult which also indicated in the reported literature.[13] Therefore, we have taken an average value of 0.04 mF.cm^{-2} for all ECs measured for 1 M KOH to determine the ECSA on the basis of an extensive literature survey.[14-17]

The roughness factor (R_f) of the ECs is calculated by the Eq. S2,[10,13,18]

$$\mathbf{R_f} = \frac{\mathbf{ECSA}}{\mathbf{GSA}} \tag{S16}$$

Here, GSA is the geometric surface area of the electrode (0.071 cm^2).

The mass activity ($A.g^{-1}$) of all ECs is acquired from the measured current density j ($mA.cm^{-2}$) by the catalyst loading m ($mg.cm^{-2}$).[10,19,20]

$$\textbf{Mass Activity} = \frac{\mathbf{j}}{\mathbf{m}} \tag{S17}$$

For OER, the turnover frequency (TOF) is determined through the following equation:[21-22]

$$\textbf{TOF} = \frac{\mathbf{js}}{\mathbf{4Fn}} \tag{S18}$$

Where, j is the obtained current density ($A.cm^{-2}$) at η of 200 mV, S is the surface area (cm^2) of the electrode with active catalyst, the number 4 suggests 4 electrons transfer during OER, F is Faraday constant (96485 C mol^{-1}), and n is the number of moles of the catalytic material on the working electrode. It represents the number of moles of O_2 molecules evolved per second per mole of EC, offering valuable perception about the per-site activity of the ECs. Herein, we assume that all metal atoms are involved in OER.

Subsequently, TOF for HER can be determined with the following equation:[10,23]

$$\textbf{TOF} = \frac{\mathbf{I}}{\mathbf{2Fn}} \tag{S19}$$

Where, I is the current of polarization curve in A at η of 83 mV. Here, the factor 2 signifies the required two electrons for the formation of one H_2 molecule in HER.

S4. OER mechanism

During OER, 4 e^-s needs to be transferred for per O_2 molecule generation and this e^- transfer may be occurred through multiple steps. The theoretical thermodynamic voltage for multistep 4 e^- oxidation processes is 1.23 V. The widely accepted whole OER process which consists of four elementary steps can be ascribed below.[10,13,24]

In alkaline media:

Step-I $$'*' + OH^- \rightarrow OH^* + e^- \tag{S20}$$

Step-II $$OH^* + OH^- \rightarrow O^* + H_2O + e^- \tag{S21}$$

Step-III $$O^* + OH^- \rightarrow HOO^* + e^- \tag{S22}$$

Step-IV $$HOO^* + OH^- \rightarrow O_2 + H_2O + e^- + '*' \tag{S23}$$

Overall Reaction:

$$4OH^- \rightarrow O_2 + H_2O + 4e^- \tag{S24}$$

Here '*' infers the active sites of the EC and during 4-step process, the generated three reaction intermediates OH^*, O^*, and HOO^* represent the adsorbed oxygen-containing species on the catalysts surface. Typically, during the electrochemical oxidation condition, the oxidation of OH^- ions is initiated to form OH^* in step I, followed by deprotonation in step II and then further oxidation for the generation of the oxygenated intermediate of HOO^*, and finally O_2 will release in step IV.

S5. HER mechanism

During HER, only 2 e$^-$ are transferred for releasing one H_2 molecule and a theoretical thermodynamic voltage of 0 V is required to drive the HER. Typically, it is a two-step 2 e$^-$ process which is expressed by the following equations (in alkaline media):[10,25]

Step-I

$$'M' + H_2O + e^- \rightarrow M - H_{ads} + OH^- \qquad \text{(S25)}$$

$$(\text{Volmer Reaction}, \sim 120\ \text{mV dec}^{-1})$$

Step-II

$$M - H_{ads} + H_2O + e^- \rightarrow 'M' + H_2 + OH^- \qquad \text{(S26)}$$

$$(\text{Heyrovsky reaction}, \sim 40\ \text{mV dec}^{-1})$$

Or

$$2M - H_{ads} \rightarrow 2'M' + H_2 \qquad \text{(S27)}$$

$$(\text{Tafel reaction}, \sim 30\ \text{mV dec}^{-1})$$

Overall Reaction:

$$2H_2O + 2e^- \rightarrow H_2 + 2OH^- \qquad \text{(S28)}$$

Here, M and H_{ads} represent the metal atom (active center) of the EC and the H atom chemically adsorbed at the active center, respectively. The Tafel slopes of the above steps are 120, 40, and 30 mV dec^{-1}, respectively. In accordance with the aforementioned steps, the adsorbed hydrogen intermediate (H_{ads}) is initially formed in the Volmer step (step I). Here, these hydrogen ions are originated from the cleaved water molecules. In step II, H_2 molecules are produced that involves two different routes. One (in Heyrovsky step) is combination of one proton with the H_{ads} species generated from step I to provide an H_2 molecule. And in the other route named as Tafel step, two as-formed H_{ads} species (in step I) are directly combined to generate an H_2 molecule. Thus, the Tafel slopes can easily establish the reaction mechanism of HER, mostly including the Volmer-Heyrovsky or Volmer-Tafel mechanism.

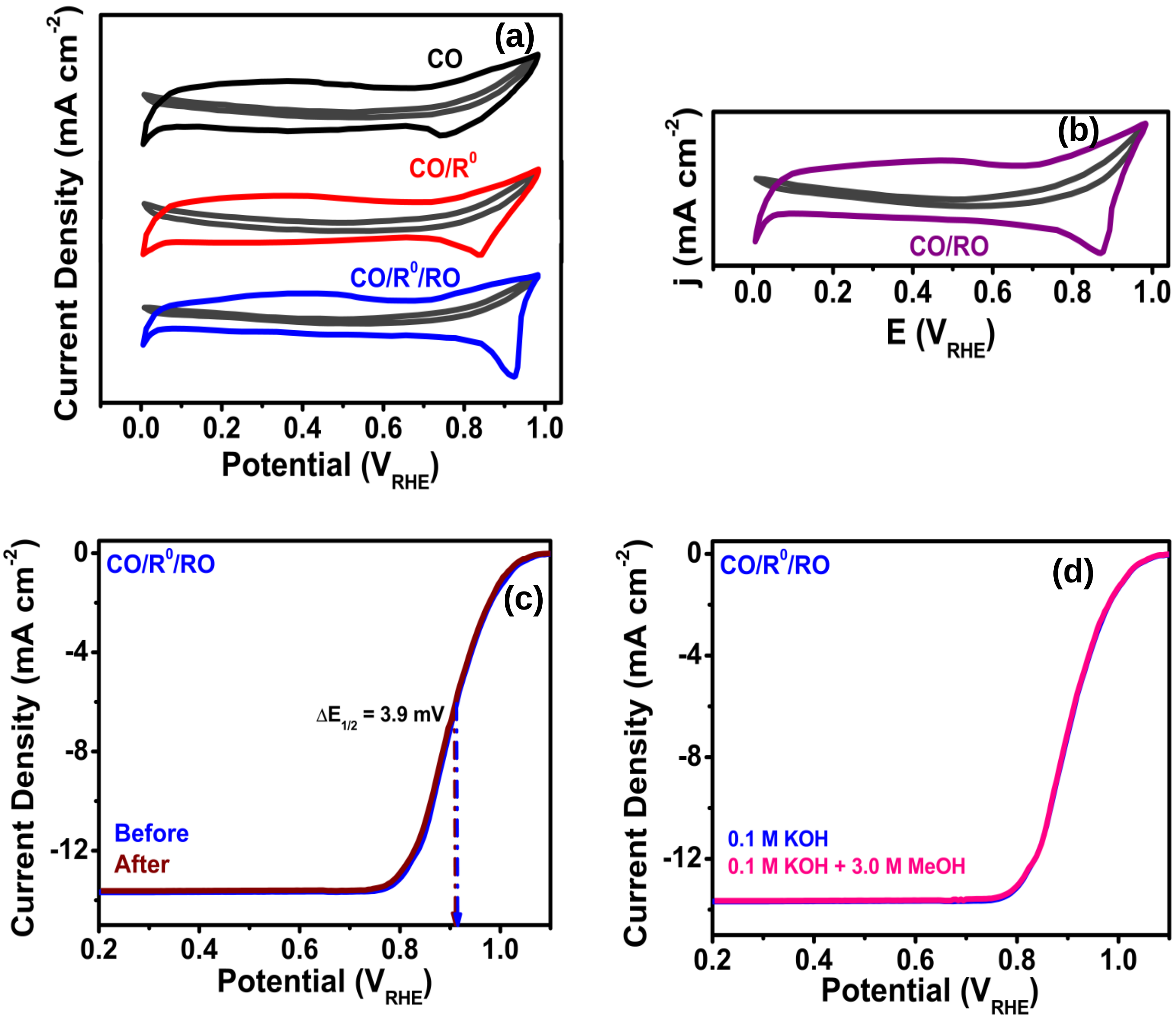

Fig. S14 ORR performances: CV curves of (a) CO, CO/R^0, CO/R^0/RO and (b) CO/RO in the N$_2$ (dark grey) and O$_2$ saturated 0.1 M KOH solution; (c) cycling stability of CO/R^0/RO at the first cycle and 300000th cycle in O$_2$ saturated 0.1 M KOH solution, and (d) LSV of CO/R^0/RO with or without MeOH.

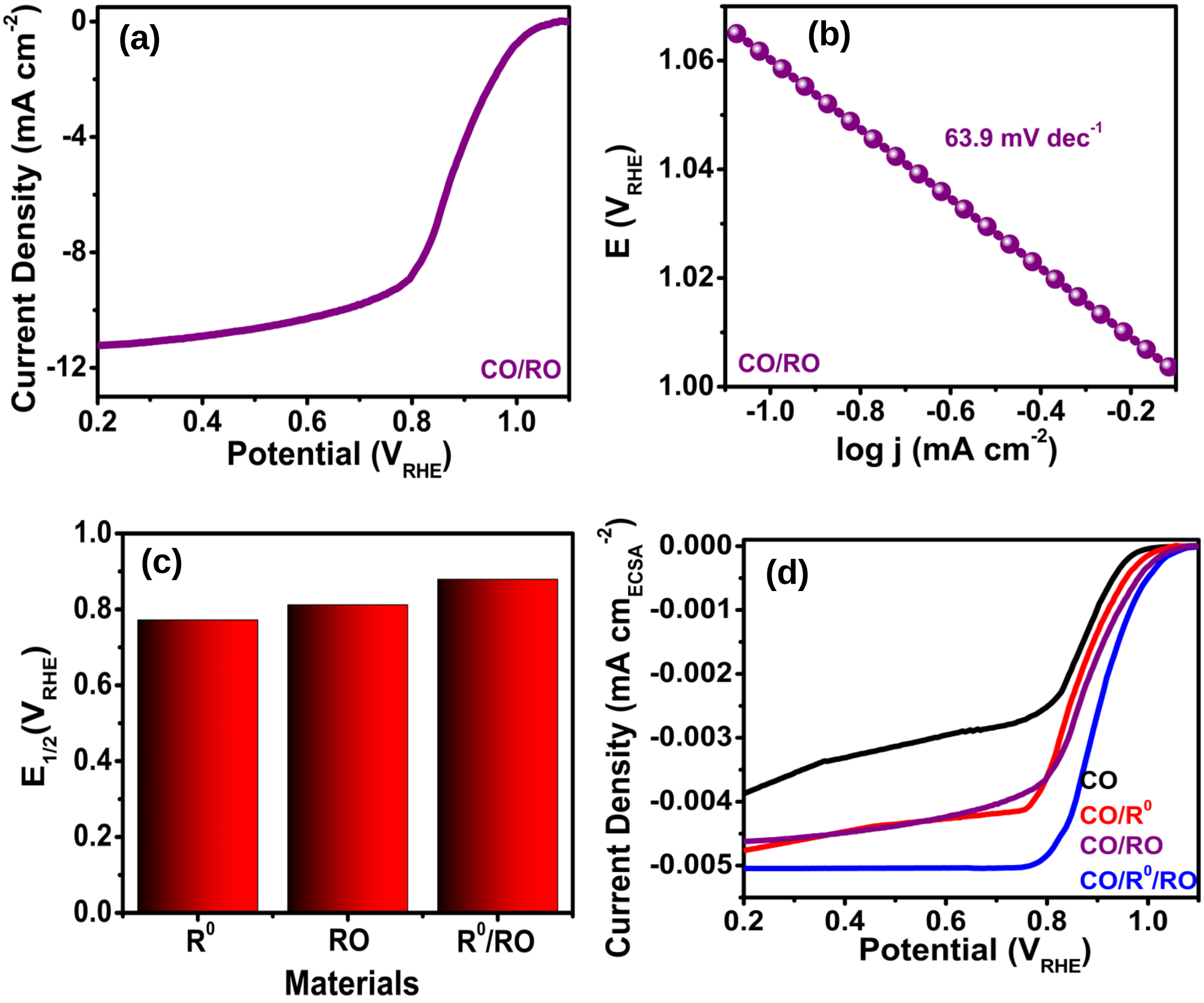

Fig. S15 (a) LSV of CO/RO during ORR under 1600 rpm rotational speed, (b) the corresponding Tafel plot of CO/RO, (c) bar diagram representing $E_{1/2}$ of R^0, RO, and R^0/RO, and (d) ECSA normalized ORR polarization curves of the synthesized catalysts.

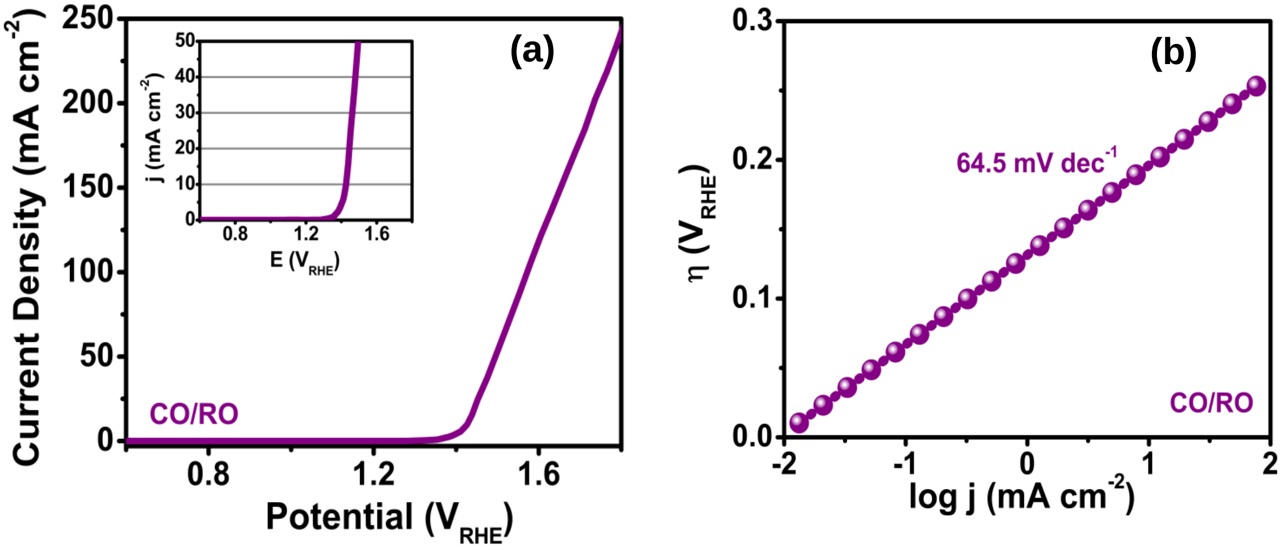

Fig. S16 LSV of CO/RO during OER under 1600 rpm rotational speed in 0.1 M KOH, and (b) the corresponding Tafel plot of CO/RO.

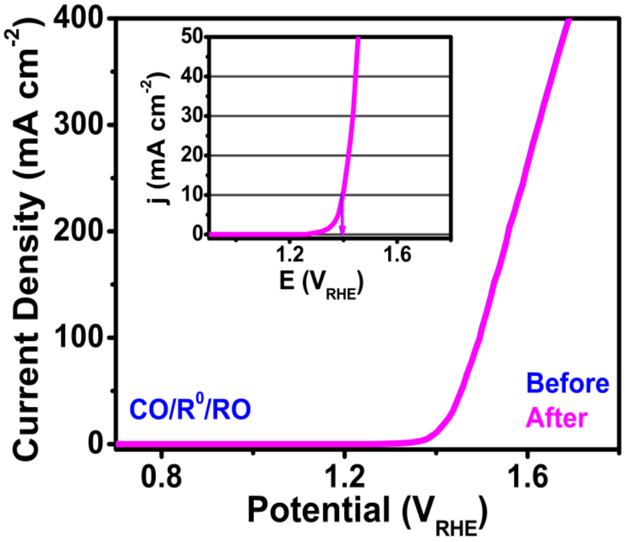

Fig. S17 OER cycling stability of CO/R^0/RO at the first cycle and 300000th cycle in 0.1 M KOH.

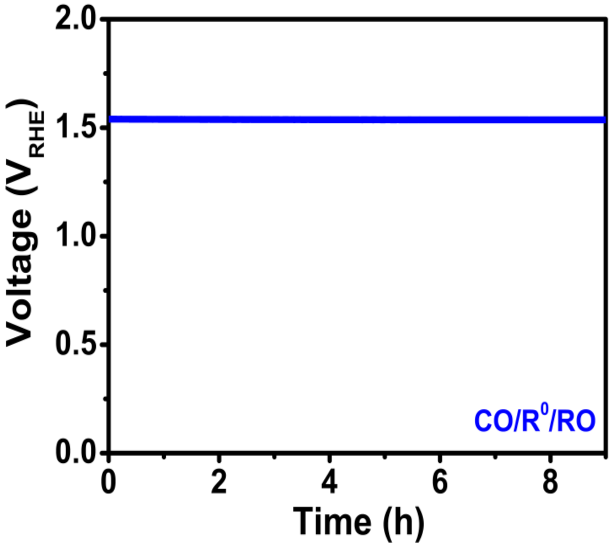

Fig. S18 Open circuit voltage of ZAB using as CO/R^0/RO cathode.

Table S6 Electrocatalytic OER/ORR performances of the ECs in 0.1 M KOH.

OER					ORR					ΔE
ECs	E_{onset} (V_{RHE})	$\eta_{j=10\ mA\ cm^{-2}}$ (mV)	j_{OER} (mA cm^{-2}) at η=320 mV	Tafel slope (mV dec^{-1})	E_{onset} (V_{RHE})	$E_{1/2}$ (V_{RHE})	j_{ORR} (mA cm^{-2}) at 0.2 V and 1600 rpm	Tafel slope (mV dec^{-1})	η = (1.23-$E_{1/2}$) (V_{RHE})	
CO	1.52	390	3.4	123.5	0.983	0.892	-6.7	73.6	0.338	0.728
CO/R^0	1.40	241	26.3	83.1	1.021	0.905	-10.4	67.3	0.325	0.566
CO/RO	1.38	190	86.9	64.5	1.036	0.914	-11.2	63.9	0.316	0.506
CO/R^0/RO	1.34	166	179.3	63.6	1.056	0.936	-13.7	53.2	0.294	0.460
RuO_2	1.51	343	5.3	85.1						0.729
Pt/C					1.000	0.844	-5.8	69.0	0.386	

Table S7 Electron transfer number (n) and peroxide yield during ORR.

ECs	$n_{K\text{-}L}$ (0.2V-0.7 V)	n_{RRDE} (0.2V-0.7 V)	H_2O_2 (%) (RRDE)
CO/R^0/RO	4.0	~4.0	0.82

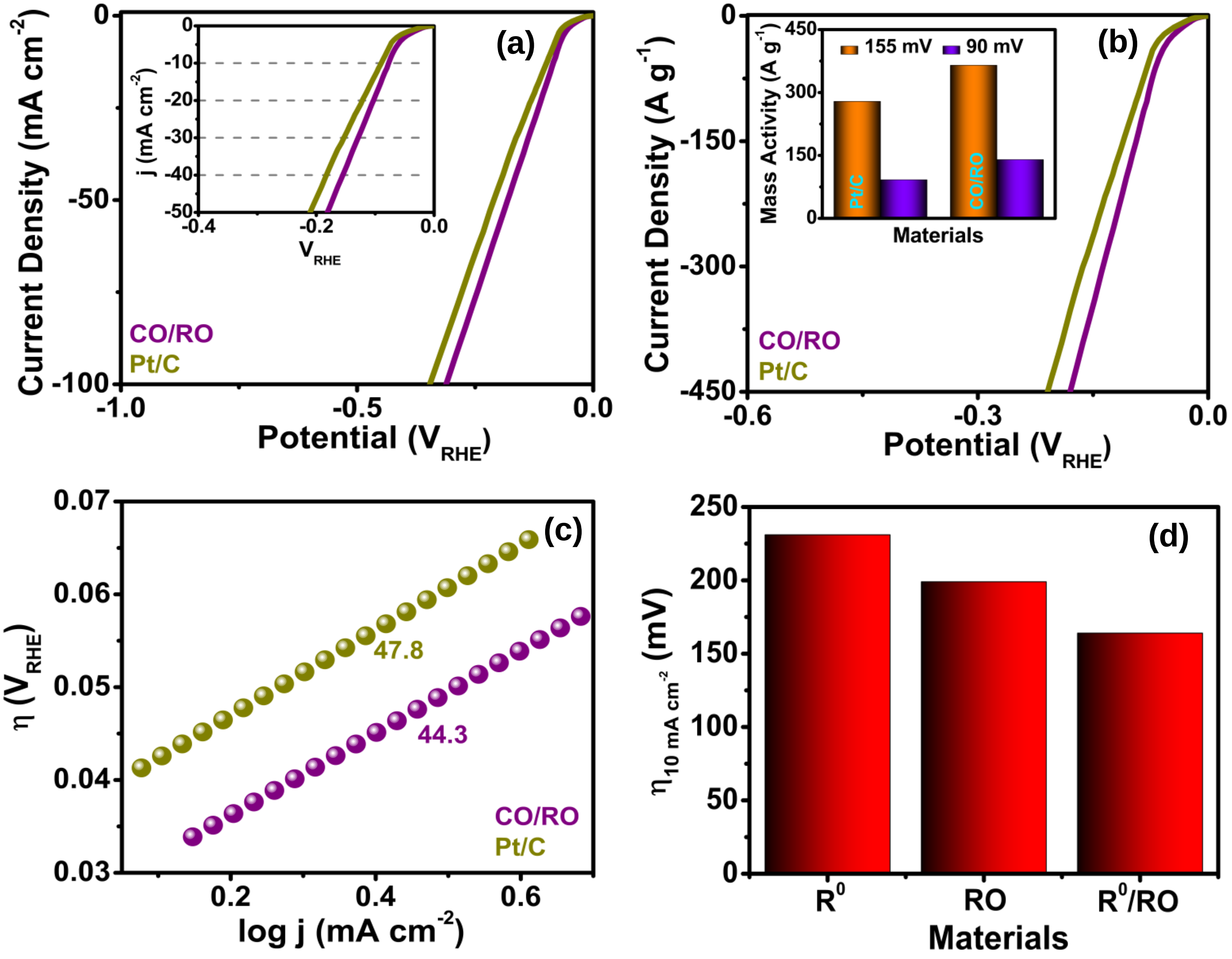

Fig. S19 (a) HER polarization curves (inset: LSV plots up to current density of -50 mA cm^{-2}), (b) mass activity plots (inset: bar diagram representing mass activity at $\eta = 155$ and 90 mV), (c) HER Tafel plots of CO/RO, and Pt/C, and (d) bar diagram representing HER $\eta_{10\ \mathrm{mA.cm}^{-2}}$ of R^0, RO, and R^0/RO.

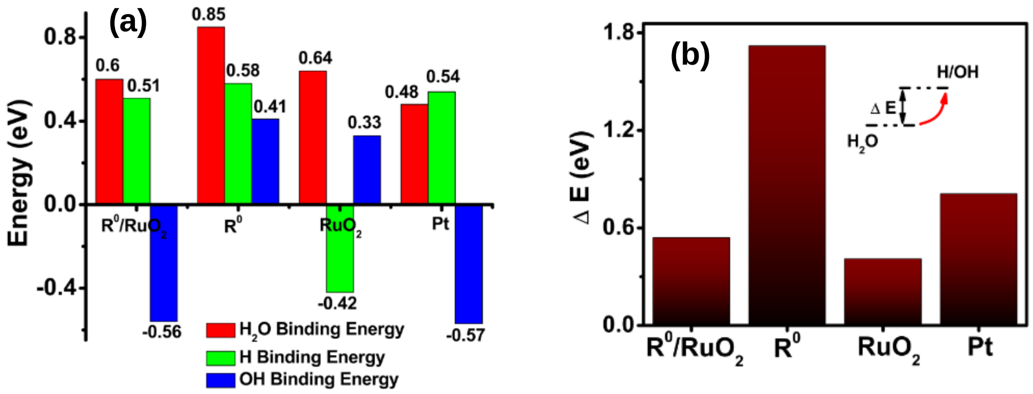

Fig. S20 (a) Theoretical calculation of binding energy on R^0/RuO_2, R^0, RuO_2 and Pt catalysts surface for H_2O, H and OH, respectively, and (b) adsorbed H_2O dissociation configuration on the surfaces of R^0/RuO_2, R^0, RuO_2 and Pt catalysts.[26]

S6. Mott-schottky measurements

The capacitance measurements are performed to find out the flat band potential (E_{fb}) of the materials and it is determined by the following Mott-Schottky Eq. S27.[8]

$$\frac{1}{C^2} = \frac{2}{e\varepsilon\varepsilon_0 N_D}\left(E - E_{fb} - \frac{K_B T}{e}\right) \quad \text{(S29)}$$

Here, C is the space-charge capacitance (F/cm^2), e is the electronic charge (C), ϵ is the dielectric constant of the semiconductor material, ϵ_0 is the permittivity of free space, and N_D is the carrier density (cm^{-3}); E and E_{fb} represent the applied potential and flat band potential (V) respectively, K_B is the Boltzmann constant, and T is the temperature. The extrapolation of the linear part of Mott-Schottky plot to C^{2-}=0 provides the E_{fb}.

The Mott-Schottky measurements are carried out in 1.0 M KOH solution with a scan rate of 0.05 V·s^{-1} at a frequency of 10 kHz and the AC voltage magnitude of 5 mV. The ITO coated glass slide fabricated with EC used as a working electrode during this analysis.

S6.1. Electrode preparation for Mott-Schottky measurements

First the glass slides are ultrasonically cleaned for 12 h with soap water followed by repetitive wash with acetone-isopropanol, respectively through ultrasonication for another 2 h. Then, slides are kept for drying for 1 h in hot air oven at 100^0 C. At that time, 4 mg EC is ultrasonically dispersed in 1 ml H_2O. Subsequently, this suspension is deposited on the conducting side of the slide through spin-coating and then air dried. Finally, the fabricated glass slide is heated under vacuum at 100^0 C for 2 h and used as working electrode.

Table S8 Band potentials of CO.

Materials	E_{fb} (V_{RHE})	Bang gap (eV)	E_{VB} (eV)	E_{CB} (eV)
CO	-0.44	3.00	2.56	-0.44

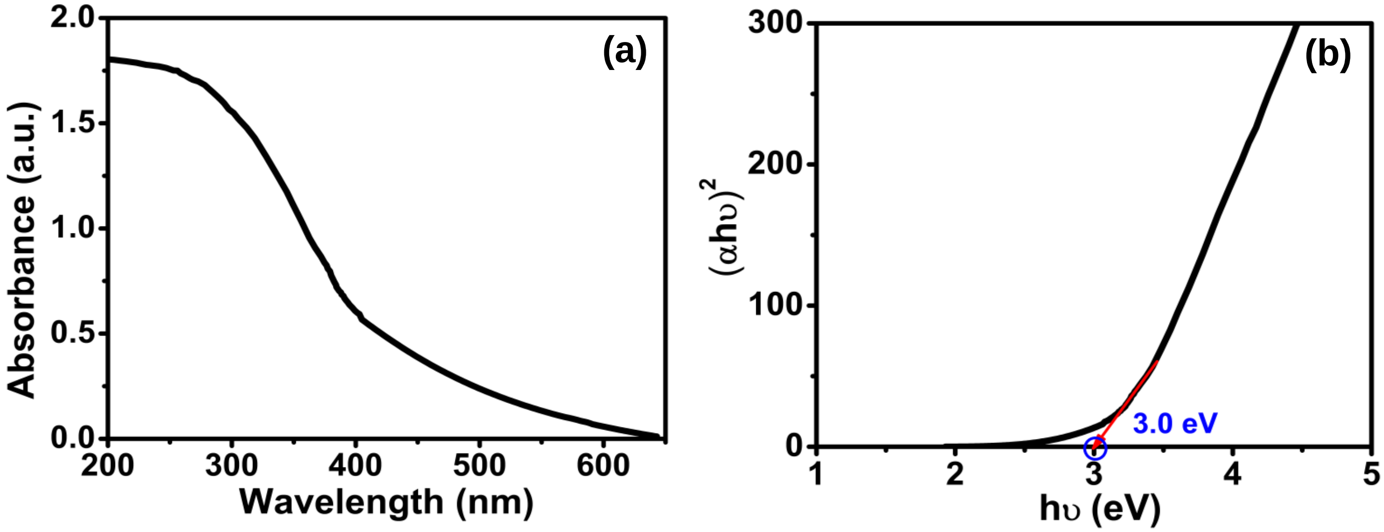

Fig. S21 (a) UV-Vis spectra, and (b) Tauc plot of CO.

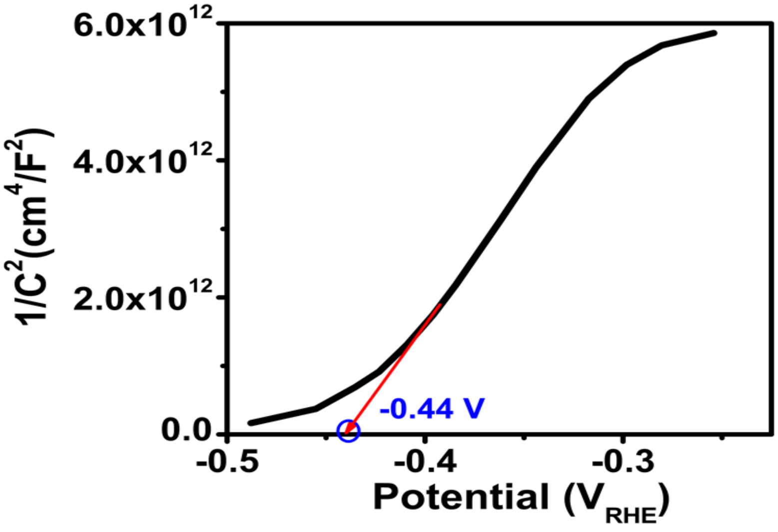

Fig. S22 Mott-Schottky plots of CO.

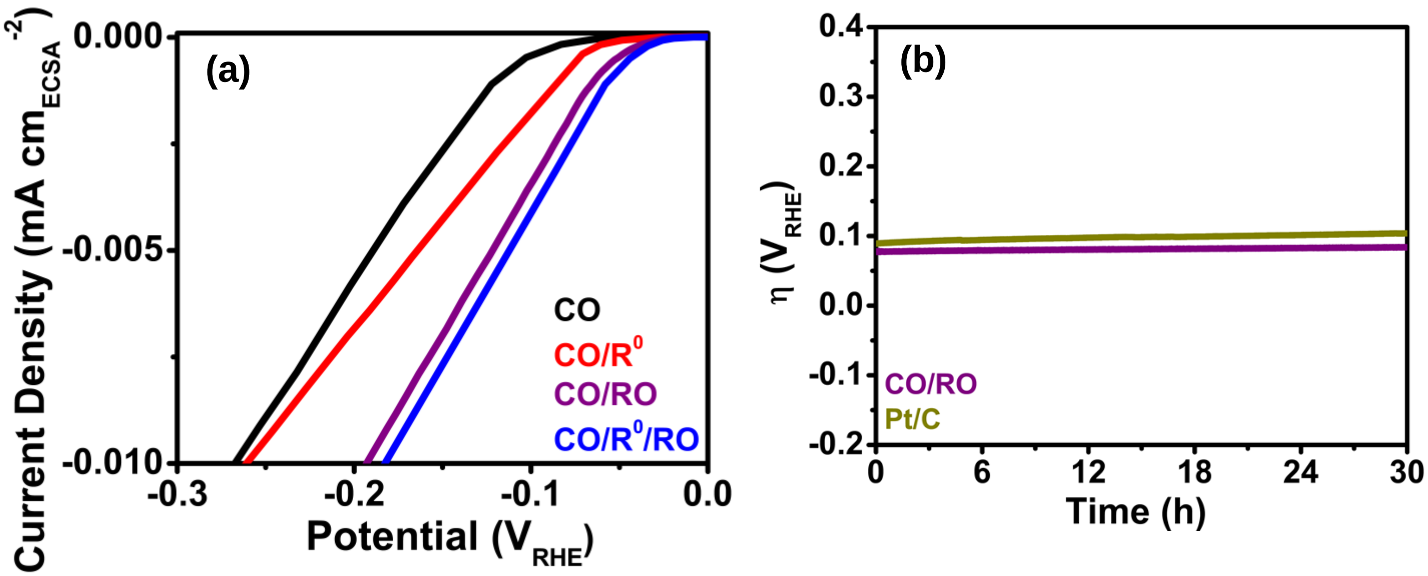

Fig. S23 (a) ECSA normalized HER polarization curves of the synthesized catalysts, and (b) chronopotentiometric stability tests (for HER) of CO/RO, and commercial Pt/C at 10 mA.cm^{-2} current density.

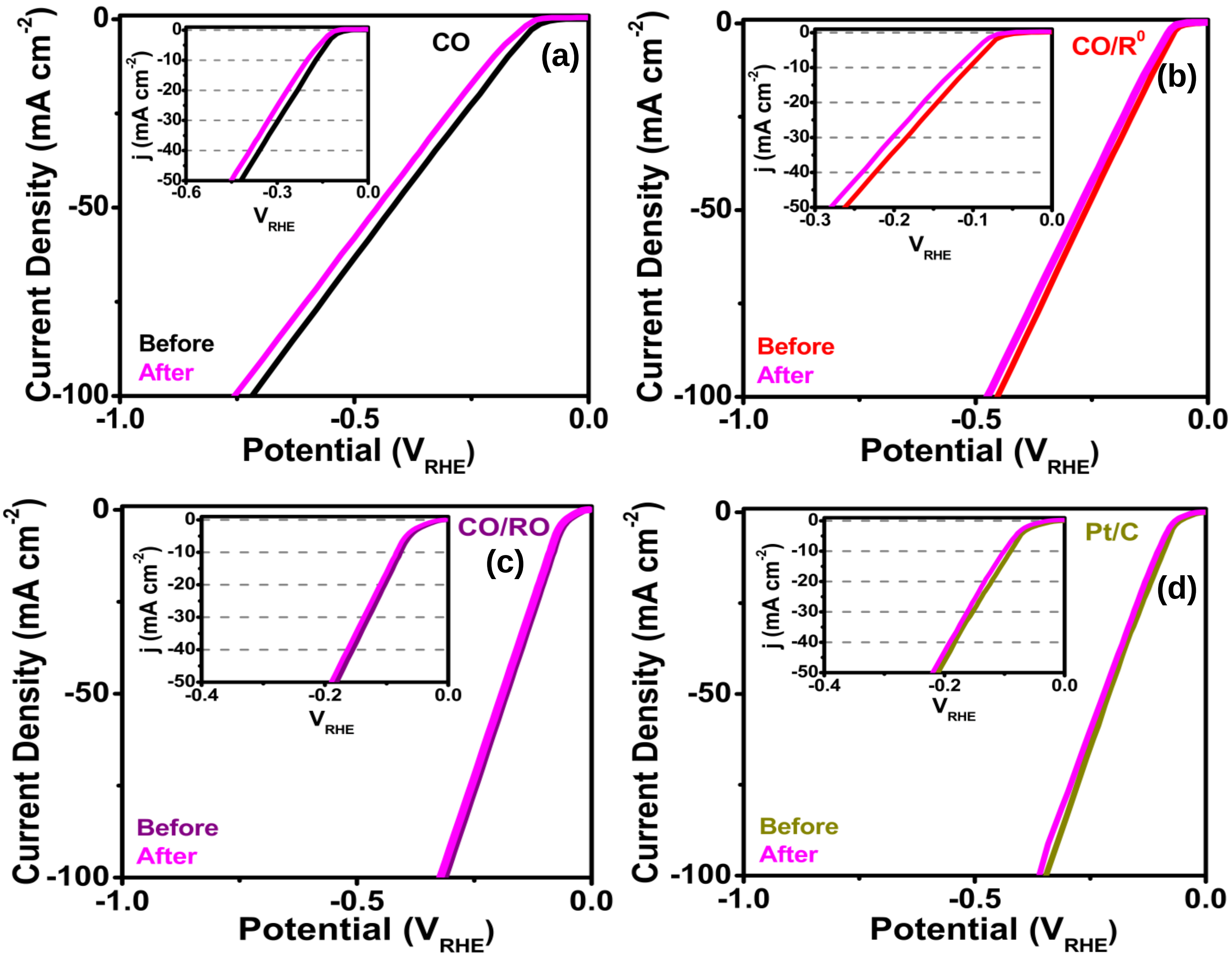

Fig. S24 HER polarization curves of (a) CO, (b) CO/R^0, (c) CO/RO, and (d) commercial Pt/C after 30h chronopotentiometric stability test [insets of (Fig. a, b, c, and d): corresponding LSV plots up to current density of -50 mA.cm^{-2}].

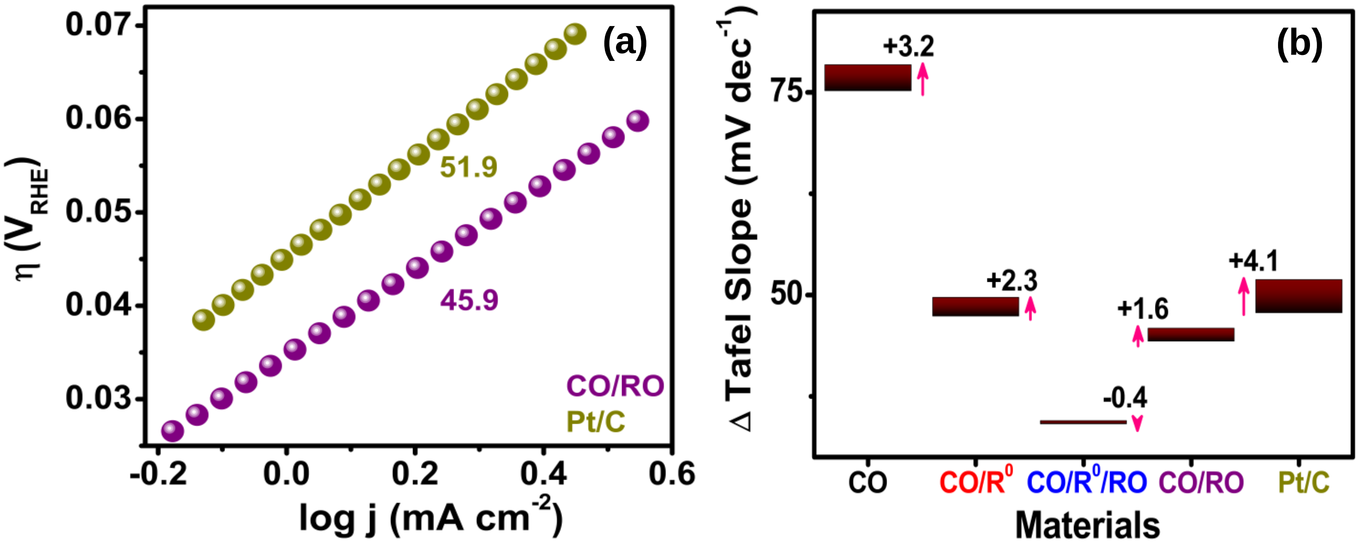

Fig. S25 (a) HER Tafel plots of CO/RO, and Pt/C after the stability test, and (b) change of Tafel slopes of the ECs between before and after 30h stability test.

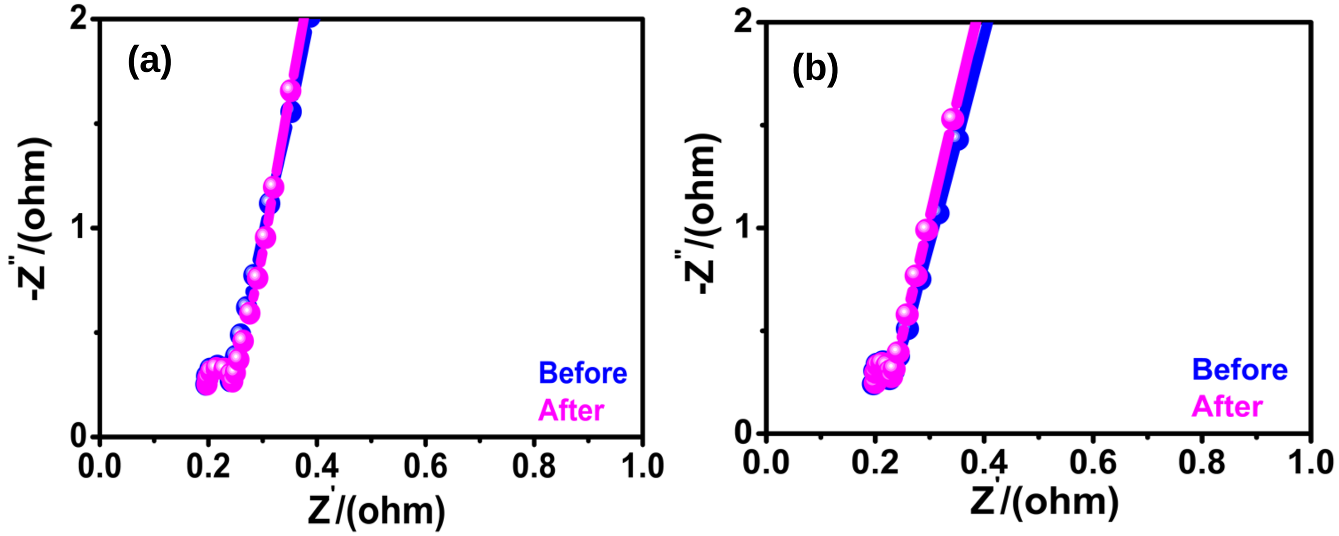

Fig. S26 EIS measurements of CO/R^0/RO before and after (a) HER, and (b) OER stability test.

Herein, the solution resistance (R_s) values for the same electrode materials and same electrolyte during OER and HER (Fig. S26a and S26b, ESI†) are different. It may be due to the differences in the reaction mechanisms, changes in ion concentration, gas evolution effects, and electrode polarization. Other reasons also include: (i) The OER and HER have different reaction kinetics which influence the current density and R_s. (ii) The production of O_2 and H_2 during OER and HER can create gas bubbles that disrupt the ionic flow near the electrode surface and alter the effective electrode area, contributing to increased R_s. (iii) In alkaline solutions, the consumption of hydroxide ions can reduce their concentration near the electrode surface, leading to increased resistance. (iv) The high positive potentials during OER lead to significant polarization of the electrode which can change the double layer structure and affect the R_s.

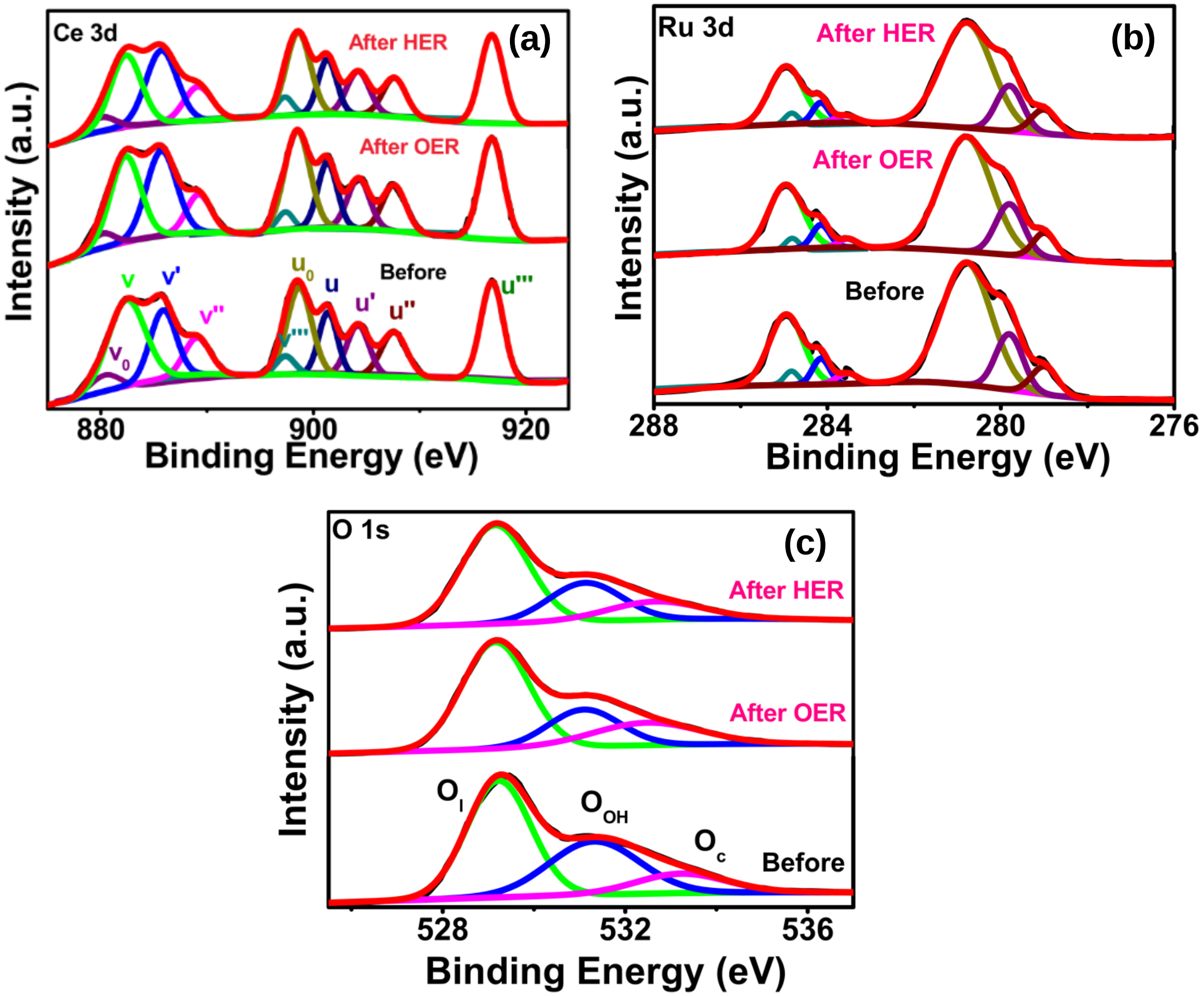

Fig. S27 (a) Ce 3d, (b) Ru 3d, and (c) O 1s XPS core level spectra of CO/R^0/RO before and after OER and HER stability test.

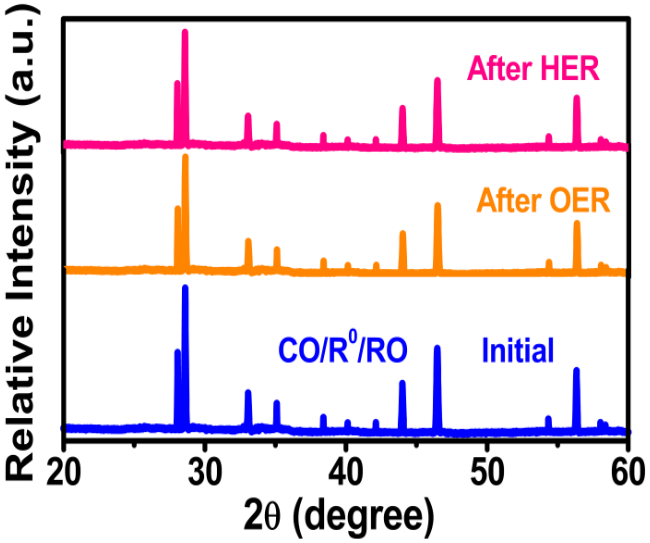

Fig. S28 Comparison of XRD of CO/R^0/RO before and after OER, and HER stability test.

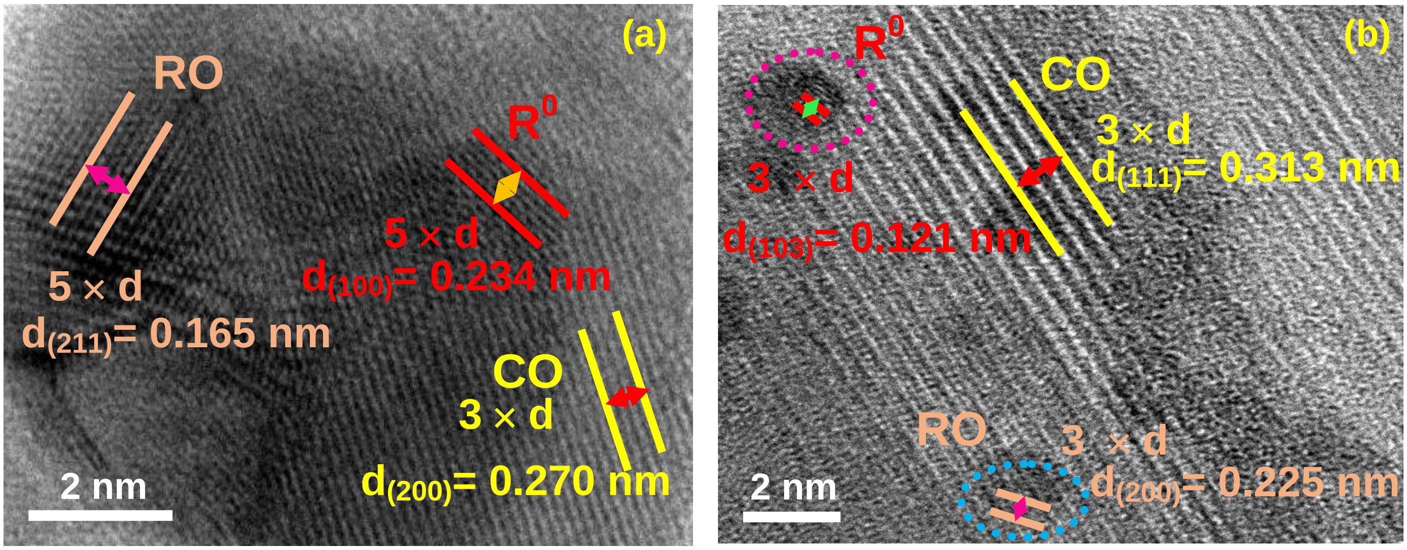

Fig. S29 Fringe pattern of CO/R^0/RO after (a) HER, and (b) OER stability test.

S7. Linear stability plot

A graphical comparison is done to scrutinize the stability of our synthesized materials where the abscissa and ordinate of that plot (Fig. 6f, main manuscript) indicates the corresponding η_{10} values at the initial stage (t=0) and after 30h of stability test, respectively. The diagonal line is the probable response for extremely active and durable catalysts while the catalyst remaining above this line implies its deactivation with time. Thus, positioned on diagonal line, toward lower η, CO/R^0/RO expresses its excellent activity along with superior durability.

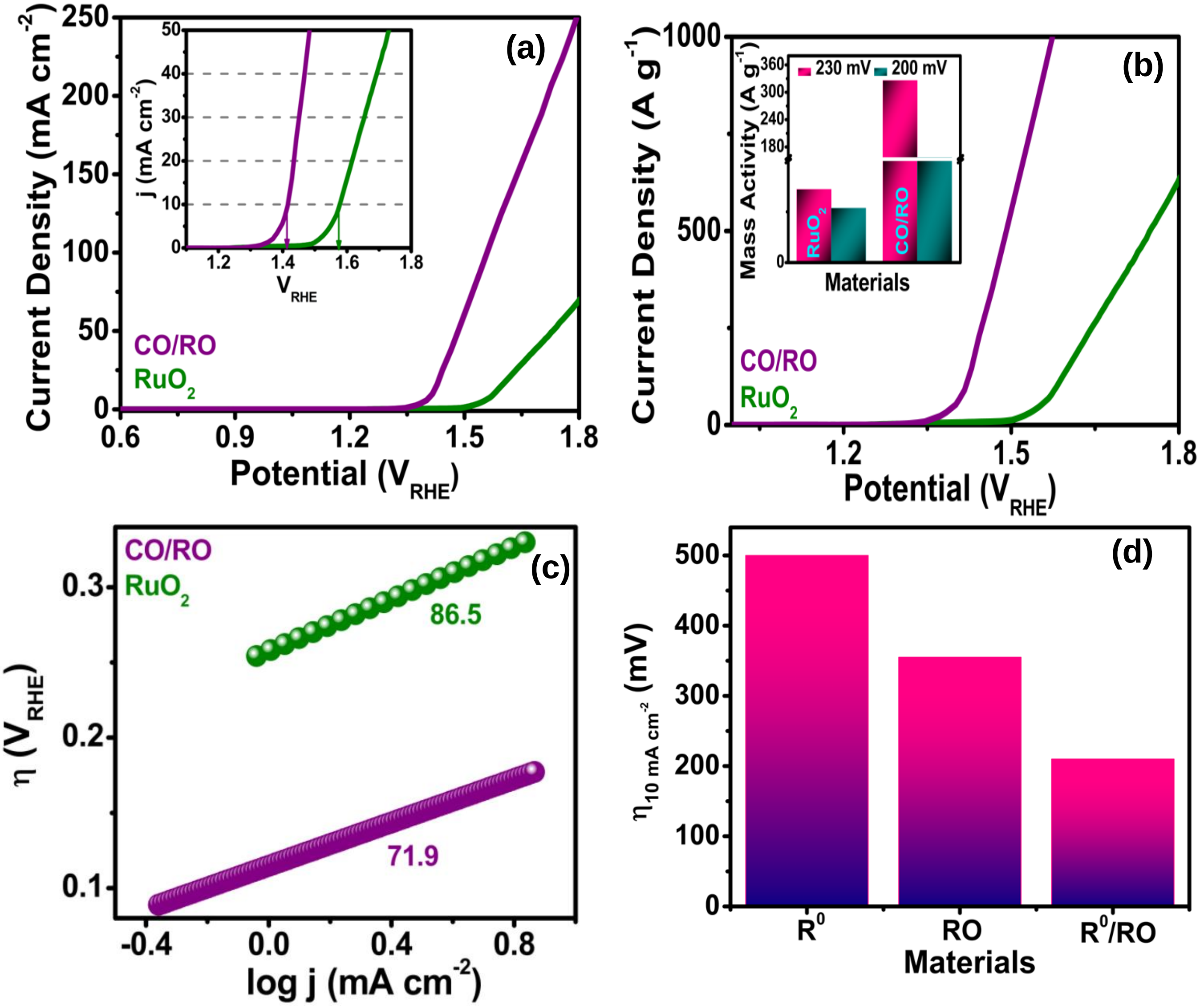

Fig. S30 OER performances in 1.0 M KOH: (a) OER polarization curves (inset: LSV plots up to current density of 50 mA.cm^{-2}), (b) mass activity plots (inset: bar diagram representing mass activity at η = 200 and 160 mV), and (c) Tafel plots of CO/RO, and commercial RuO_2; (d) bar diagram representing $\eta_{10\ mA.cm^{-2}}$ of R^0, RO, and R^0/RO.

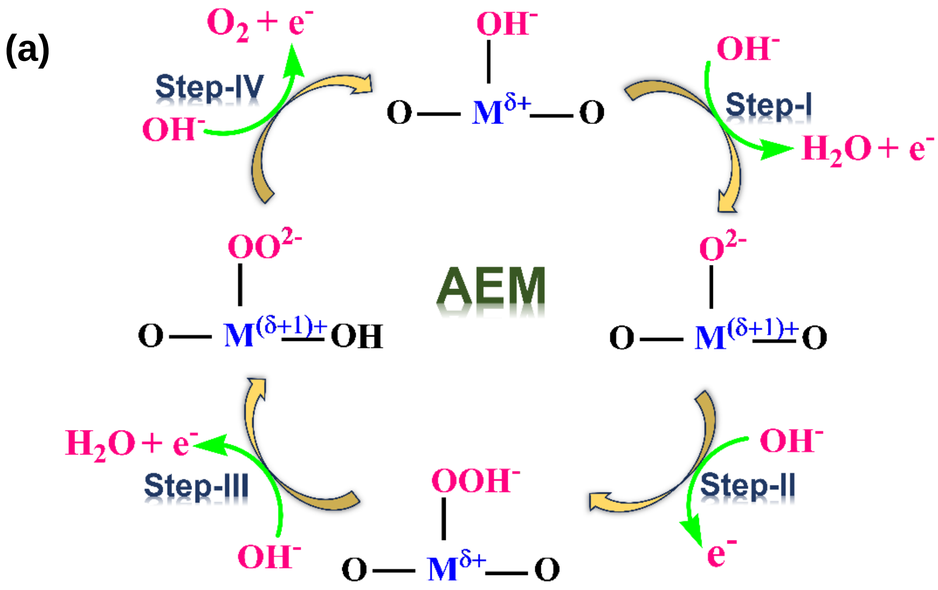
(a)
O₂ + e⁻
Step-IV
OH⁻
OH⁻
O— Mδ+—O
OH⁻
Step-I
H₂O + e⁻
OO²⁻
O— M(δ+1)+—OH
AEM
O²⁻
O— M(δ+1)+—O
H₂O + e⁻
Step-III
OH⁻
OOH⁻
O— Mδ+—O
OH⁻
Step-II
e⁻

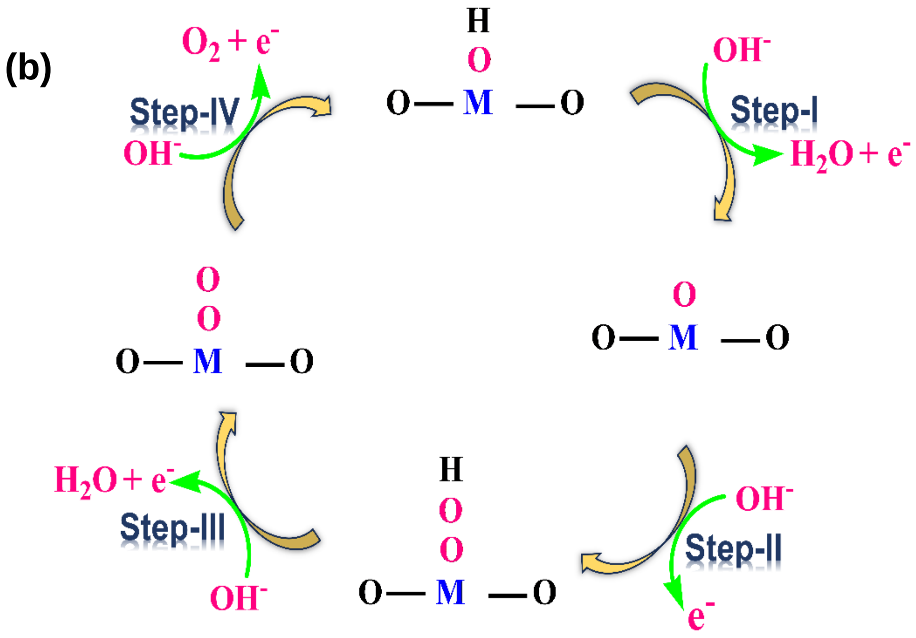
(b)
O₂ + e⁻
Step-IV
OH⁻
H
O
O— M —O
OH⁻
Step-I
H₂O + e⁻
O
O
O— M —O
O
O— M —O
H₂O + e⁻
Step-III
OH⁻
H
O
O
O— M —O
OH⁻
Step-II
e⁻

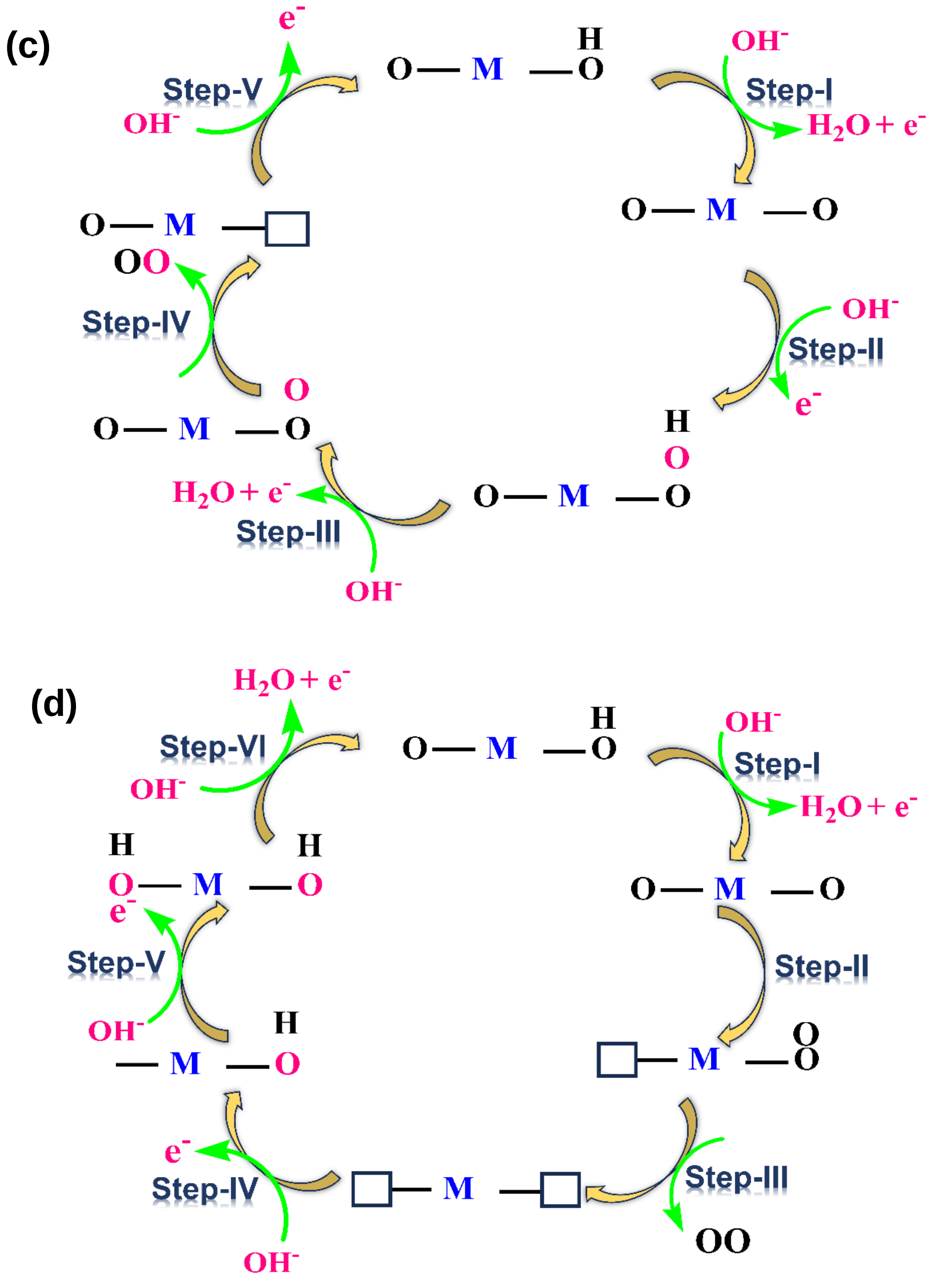

Fig. S31 (a) Well-recognized reaction paths of OER on various ECs in alkaline electrolytes. Eley-Rideal (ER) type adsorbate evolution mechanism (AEM), single metal cation ($M^{\delta+}$) is the active site, undergoes an increase in the oxidation state; (b) Conventional OER mechanism, involving concerted proton-electron transfer on surface metal sites (oxygen from electrolyte in pink, and from oxide lattice in black); (c, d) Possible mechanism of OER involving concerted proton-electron transfer on surface oxygen sites.

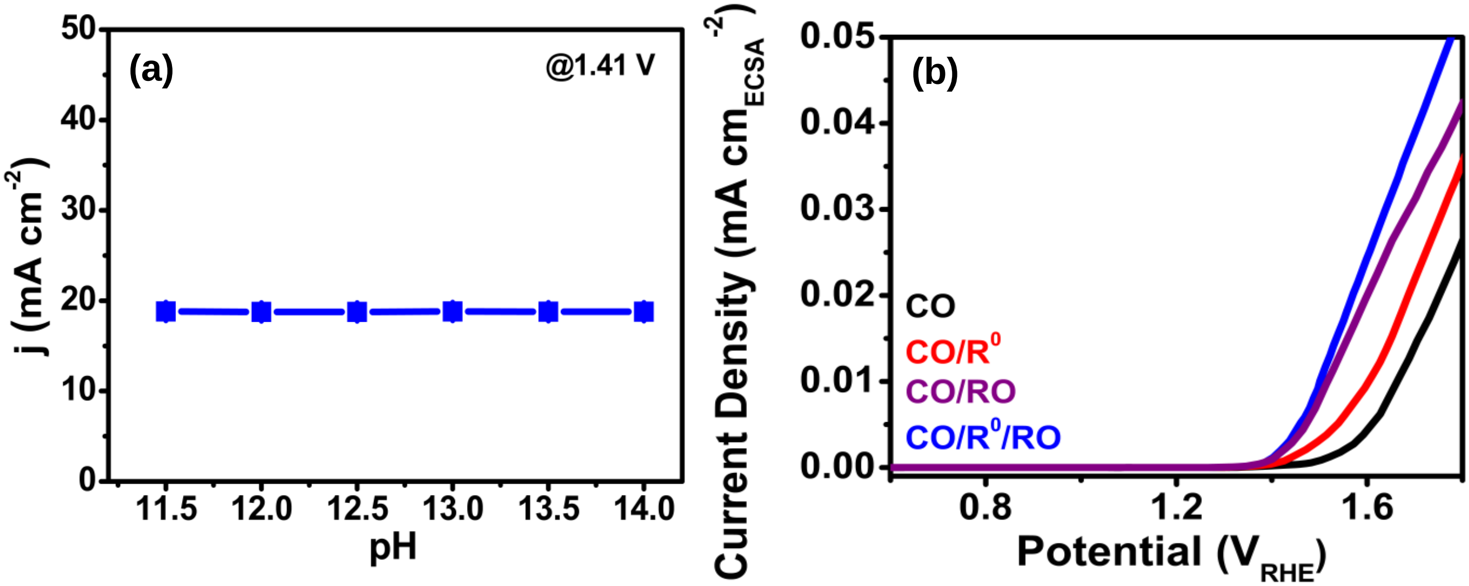

Fig. S32 (a) OER activity of CO/R^0/RO at 1.41 V as a function of pH, and (b) ECSA normalized OER polarization curves of the synthesized catalysts.

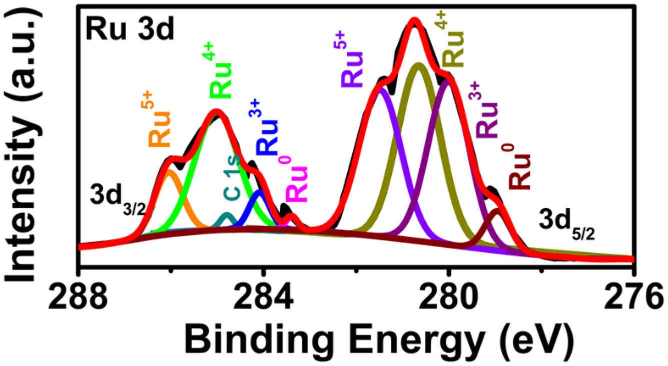

Fig. S33 In-situ XPS analysis during OER.

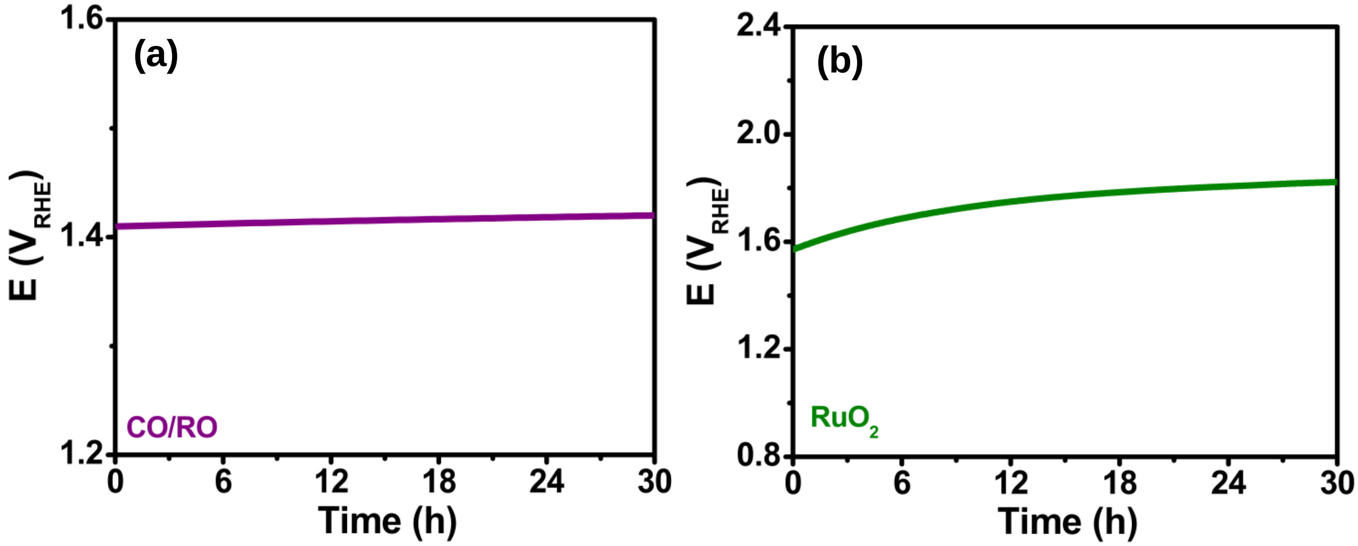

Fig. S34 Chronopotentiometric stability tests of (a) CO/RO, and (b) commercial RuO_2 at 10 $mA.cm^{-2}$ current density.

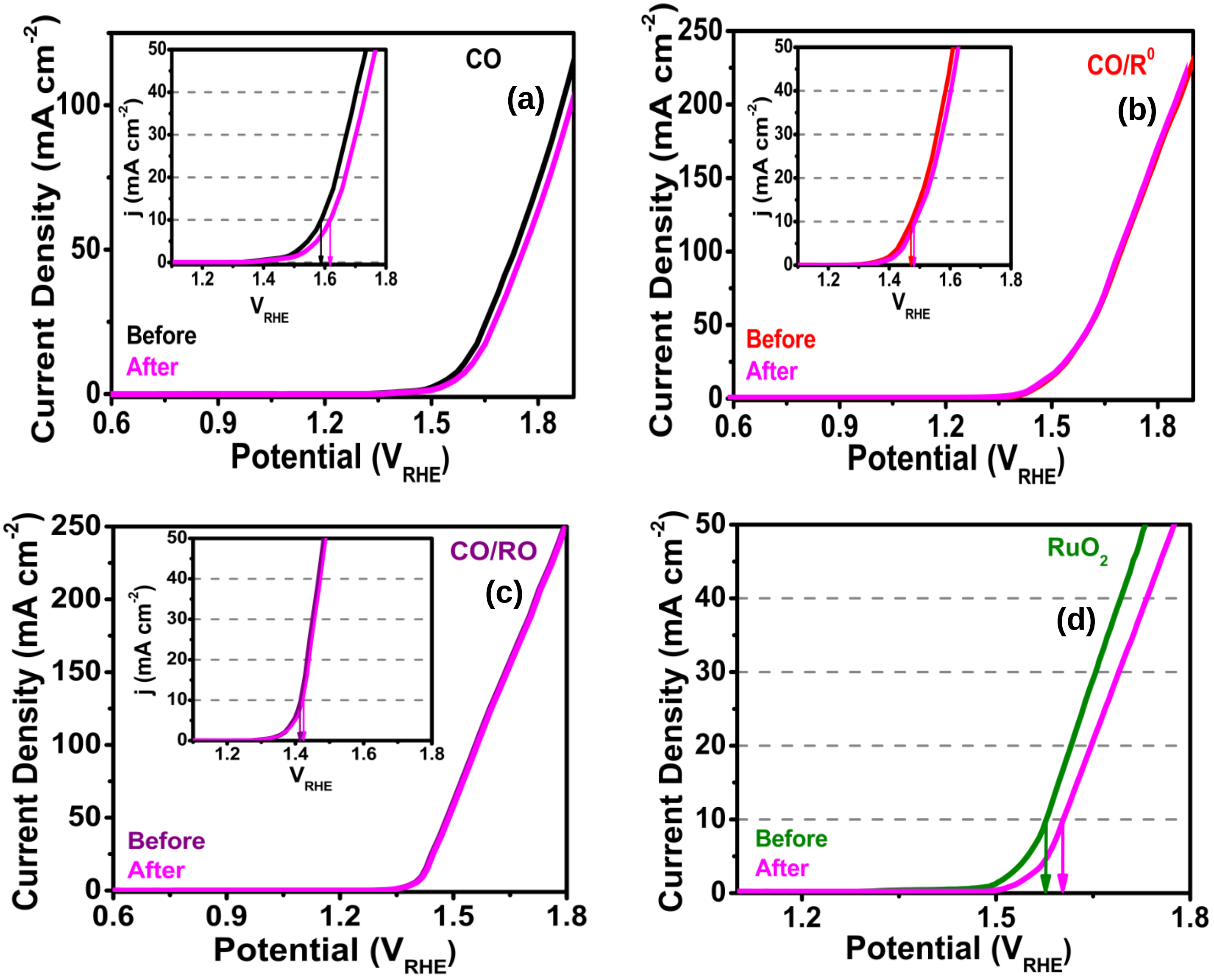

Fig. S35 OER polarization curves of (a) CO, (b) CO/R^0, (c) CO/RO, and (d) commercial RuO_2 after 30h chronopotentiometric stability test [insets of (Fig. a, b, and c): corresponding LSV plots up to current density of 50 $mA.cm^{-2}$].

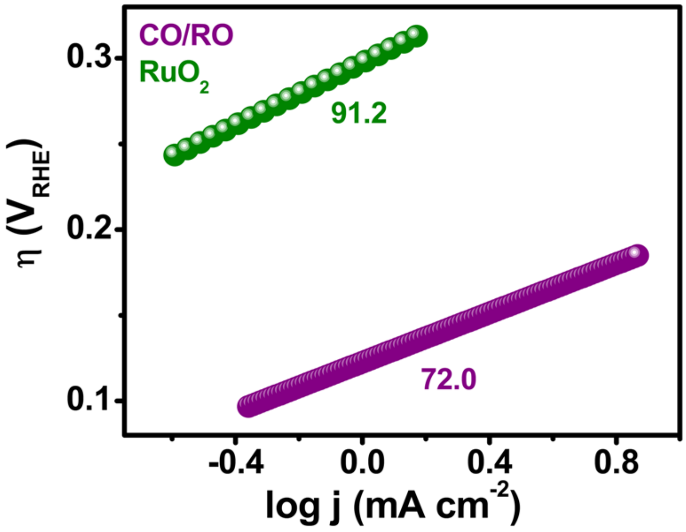

Fig. S36 OER Tafel plots of CO/RO, and RuO_2 after the stability test.

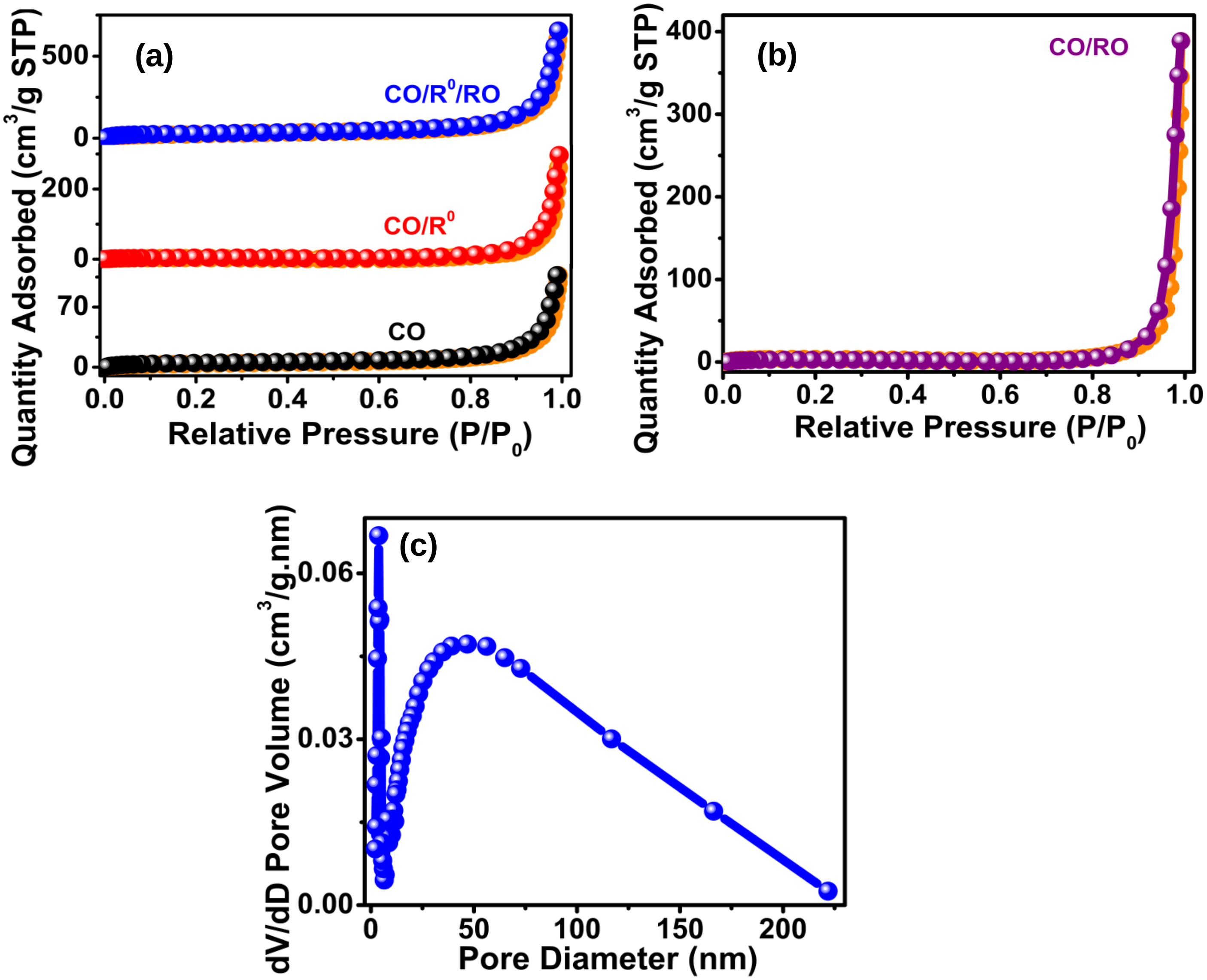

Fig. S37 BET surface area plot of (a) CO, CO/R^0, CO/R^0/RO and (b) CO/RO; (c) pore size distribution plot of CO/R^0/RO.

Table S9 BET surface area of the materials.

Materials	BET surface area (m^2/g)
CO	97.2
CO/R^0	247.8
$CO/R^0/RO$	459.5
CO/RO	296.9

S8. BET surface area analysis

As OER and HER are surface-sensitive process, it is well recognized that porous architecture with high specific area allows the EC with enhanced catalytic activity through raising the number of catalytic active sites as well as offering high electrical conductivity, enhanced charge-mass transport and close electrolyte-catalyst contact. Interestingly, it can be found that the surface area of CO is greatly enhanced after R^0 loading and this surface area is observed to increase further after RO loading over CO/R^0 (Fig. S37a, ESI†). Alternatively, CO/RO possesses surface area greater than CO/R^0 but lesser than $CO/R^0/RO$ (Fig. S37b, ESI†). This result strongly suggests that increase the number of coexistences of Ru with multivalent (M_V) oxidation states leads to increase surface area. The order of specific surface area (Table S9, ESI†) is: $CO<CO/R^0<CO/R^0/RO>CO/RO$ and this result probably contribute to the increased ECSA of $CO/R^0/RO$ [Table (S10-S12), ESI†]. Thus, the strategically designed porous $CO/R^0/RO$ may provide abundant active sites resulting an enhancement of its electrocatalytic performance.

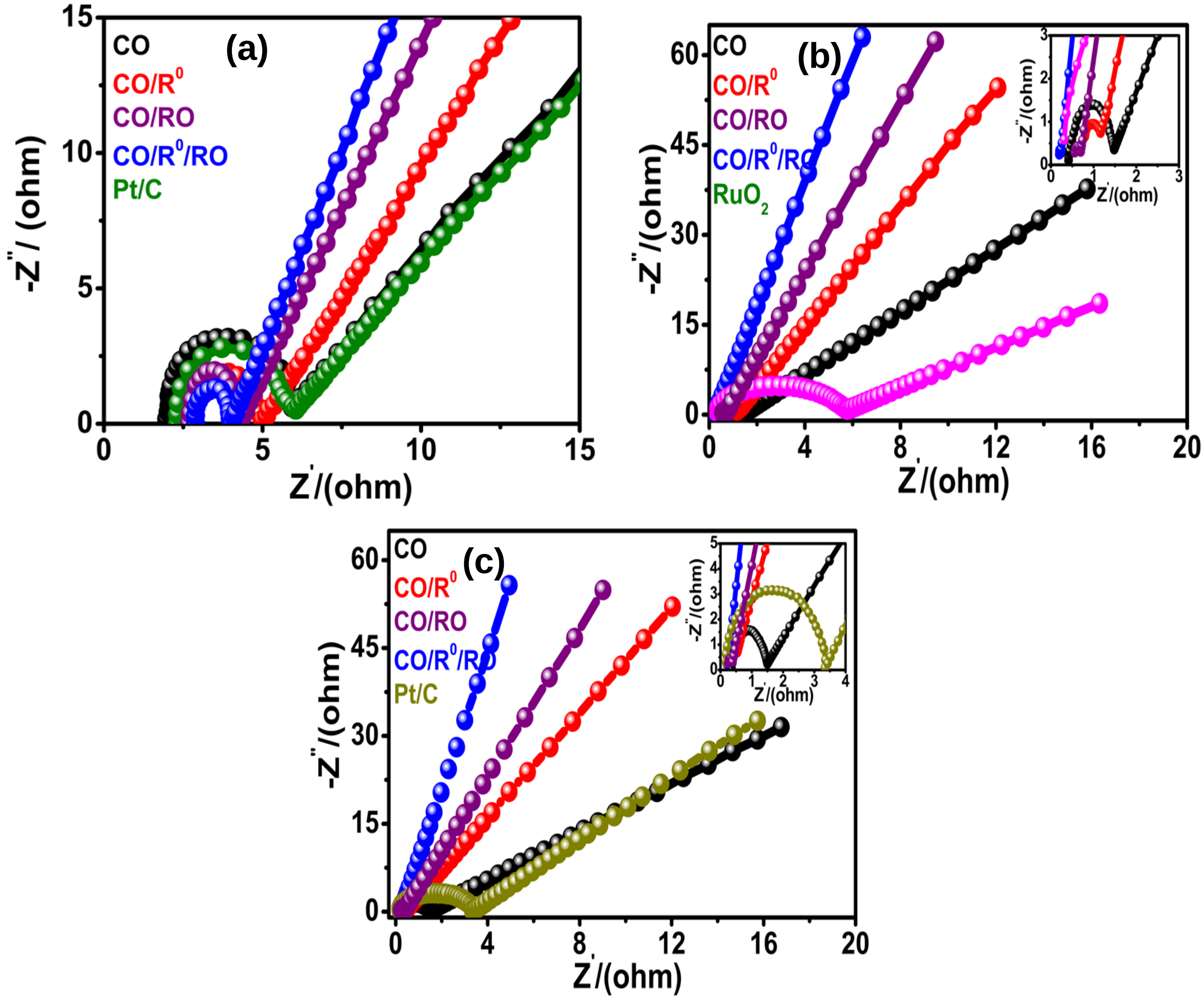

Fig. S38 Comparison of EIS of the ECs at (a) E of 1.0 V in ORR (0.1 M KOH), (b) η of 120 mV in OER (1.0 M KOH), and (c) η of 60 mV in HER (1.0 M KOH) region.

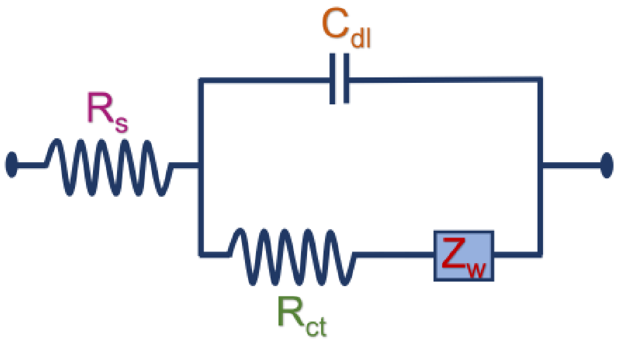

Fig. S39 The Randles cell model equivalent circuit.

Table S10 Surface parameters of the materials during ORR.

ECs	Mass loading ($\mu g\ cm^{-2}$)	Charge transfer resistance (R_{ct}) (Ω)	Double layer capacitance (C_{dl}) (mF cm^{-2})	ECSA (m^2/g)	Roughness factor (R_f)
CO	~110	3.96	4.9	111.3	1725.3
CO/R^0		2.4	6.2	140.9	2183.1
CO/RO		1.55	6.9	156.8	2429.6
CO/R^0/RO		1.11	7.7	175.0	2711.2
Pt/C		3.68	5.4	122.7	1901.4

Table S11 Surface parameters of the materials during OER.

ECs	Mass loading ($\mu g\ cm^{-2}$)	Charge transfer resistance (R_{ct}) (Ω)	Double layer capacitance (C_{dl}) (mF cm^{-2})	ECSA (m^2/g)	Roughness factor (R_f)
CO	~110	1.08	7.9	179.5	2781.7
CO/R^0		0.37	13.4	304.5	4718.3
CO/RO		0.15	17.1	388.6	6021.1
CO/R^0/RO		0.03	29.2	663.6	10281.7
RuO_2		5.49	4.4	100.0	1549.3

Table S12 Surface parameters of the materials during HER.

ECs	Mass loading ($\mu g\ cm^{-2}$)	Charge transfer resistance (R_{ct}) (Ω)	Double layer capacitance (C_{dl}) (mF cm^{-2})	ECSA (m^2/g)	Roughness factor (R_f)
CO	~110	1.14	7.2	163.6	2535.2
CO/R^0		0.33	14.1	320.4	4964.8
CO/RO		0.17	15.5	352.3	5457.7
CO/R^0/RO		0.07	25.4	577.3	8943.6
Pt/C		3.18	5.6	127.3	1971.8

S9. Electrochemical impedance spectroscopy (EIS)

To better understand the ORR/OER/HER mechanism, we assessed the intrinsic properties of the as-prepared materials by performing EIS measurements at E of 1.0 V_{RHE} for ORR (Fig. S38a, ESI†), η of 120 mV for OER (Fig. S38b, ESI†), and η of 60 mV for HER (Fig. S38c, ESI†). Herein, the Nyquist plots (Fig. S39, ESI†) provide deeper insight about the solution resistance (R_s), charge transfer resistance (R_{ct}), and double layer capacitance (C_{dl}). The charge transfer resistance (R_{ct}) is associated with the electrocatalytic kinetics at the interface of electrolyte and EC. Table (S10-S12) (ESI†) show that our CO/R^0/RO delivers a much lower R_{ct} value than CO, CO/R^0, and CO/RO during ORR, OER and HER which may a clear indication of its higher electrical conductivity. The steeper slope in low frequency region of EIS [inset of Fig. S38(b,c), ESI†] measurements of CO/R^0/RO imply a rapid diffusion of OH^- ions into the pores of the EC. Thus, R^0 and subsequent RO loading over CO improve the electrical conductivity as well as facilitate the ion diffusion to the redox active sites of CO/R^0/RO. Besides the strong interfacial interaction among CO, R^0, and RO enhances the favorable charge transfer between CO/R^0/RO and active species of the electrolyte.

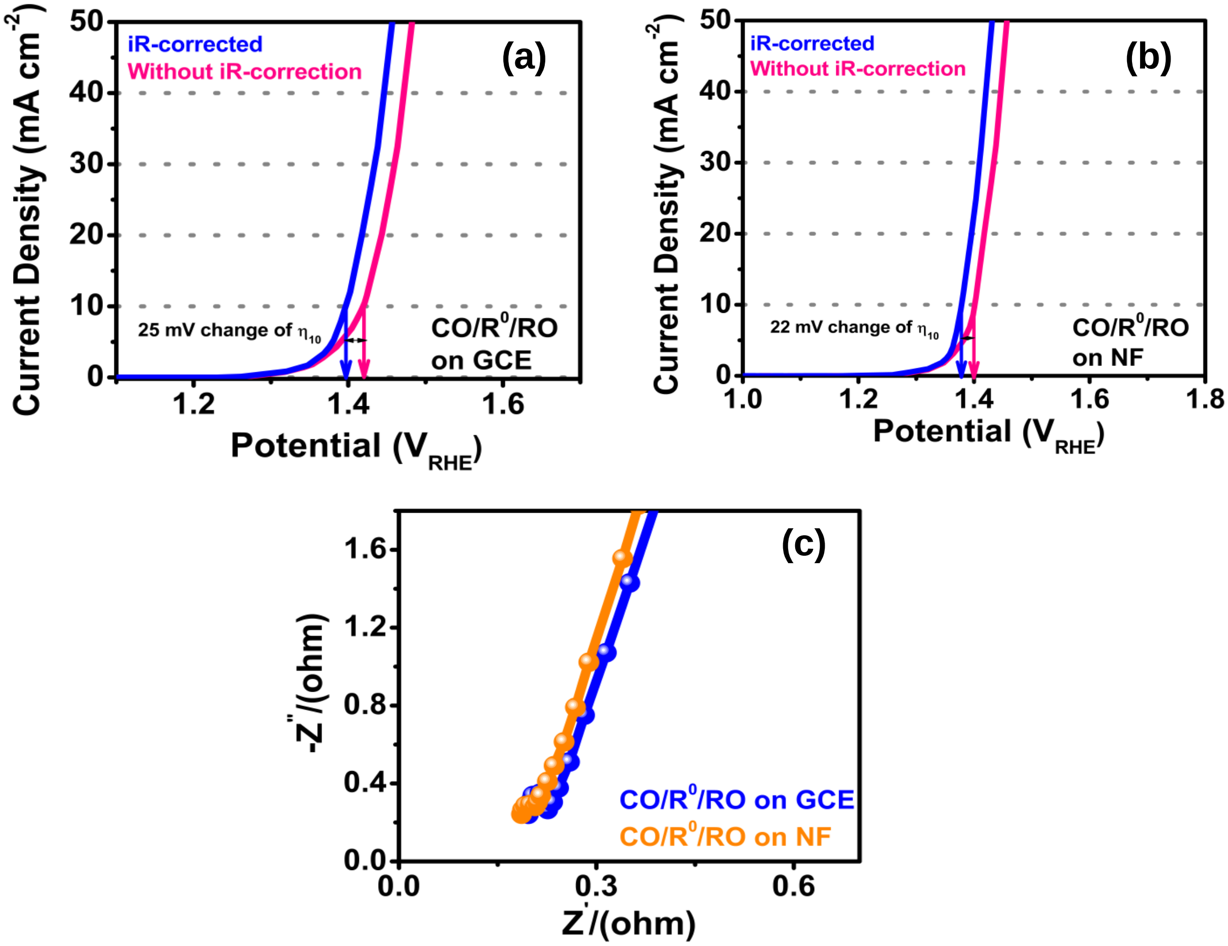

Fig. S40 (a) LSV curves of CO/R^0/RO on glassy carbon (GC) based electrode with 95%-iR correction, (b) LSV curves of CO/R^0/RO on Ni foam (NF) with 95%-iR correction, and (c) EIS of CO/R^0/RO on GC and NF based electrodes.

Table S13 Comparison of electrocatalytic ORR activity of $CO/R^0/RO$ with recently reported ECs in 0.1 M KOH solution.

	Materials	E_{onset} (V_{RHE})	$E_{1/2}$ (V_{RHE})	Tafel slope (mV dec^{-1})	N	Mass loading (mg cm^{-2})	References
	$CO/R^0/RO$	1.056	0.936	53.2	4.0	~0.11	This work
Ru-based ECs	Rh_6Cu_1/C	—	0.85	55.0	—	~0.282	27
	$RuCoO_x$	—	0.855	46.7	—	~0.396	28
	$(La_{1.5}Sr_{0.5A}(Ni_{0.5}Mn_{0.5B}(Ni_{0.5}Ru_{0.5})_{B'}O_6$	0.94	0.72	—	—	~0.255	29
	Ca_2FeRuO_6	0.90	0.78	76.0	3.77	~0.704	30
	CoRu-O/A@HNC-2	0.937	0.821	—	3.90	—	31
	$Ru/NBFNiSe_2/Mo_2CT_x$	—	0.912	—	—	0.1	32
Other Meta-based ECs	CoP/C NWs	0.96	0.85	66.0	3.8	—	33
	Co@IC/MoC@PC	1.034	0.875	78.0	~4.0	~0.396	34
	$g\text{-}C_3N_4/GO$	0.984	0.859	72.0	3.9	0.407	35
	Co_3O_4/Au	0.99	0.83	51.0	4.0	0.400	36
	Fe-N-CNT/OMC	1.01	0.85	75.0	4.0	0.300	37
	3D $Fe\text{-}WO_3$ NF/NG	0.98	0.85	—	~3.97	—	38
	CuAg@Ag/N-GNS	0.94	0.85	67.0	~3.6−3.8	0.700	39
	Co_3O_{4-x} HoNPs@HPNCS	—	0.834	—	~4.0	—	40
	fct−PdFe@Pd	~0.97	~0.83	~26.0	3.9	—	41
	$\alpha\text{-}Fe_2O_3@MoS_2/NGNS$	~0.95	~0.85	73.0	3.91−3.96	~0.348	42
	$ppy/AgVO_3/porphy$	1.05	0.89	67.0	4.0	0.19	13

Table S14 Comparison of electrocatalytic OER activity of CO/R^0/RO with reported ECs.

	Materials	Electrolyte (KOH)	E_{onset} (V_{RHE})	$\eta_{j=10\ mA\ cm^{-2}}$ (mV)	Tafel slope (mV dec^{-1})	Mass loading (mg cm^{-2})	References
	CO/R^0/CO	1.0 M	1.32	120	61.3	~0.11	This Work
Ru-based ECs	Rh_6Cu_1/C	1.0 M	___	300	70.0	~0.282	27
	$RuCoO_x$	0.1 M	___	275	54.0	~0.396	28
	CoRu-O/A@HNC-2	1.0 M	1.42	253	63.8	___	31
	SiO_x/Ru	1.0 M	___	234	64	0.25	43
	RuCo-LNC-120	1.0 M	___	242	60.1	~0.5	44
	Ru/NF-2	1.0 M	1.52	330	62	0.05	45
	RuO_2/3DMNC	1.0 M	___	216.74	63.5	4.0	46
	a-$RuTe_2$ PNRs	1.0 M	___	285	62.0	0.2	47
	$RuIrO_x$	1.0 M	___	250	50.0	1.00	48
Other Metal-based ECs	AMO/PdO_x/Pd	1.0 M	1.36	160	64.9	~ 0.16	10
	ppy/$AgVO_3$/porphy	1.0 M	1.42	220	69.63	~ 0.19	13
	Co@IC/MoC@PC	1.0 M	___	277	79.0	0.5	34
	$(Co_9S_8$/N,S−DLCTs$)_{HF}$	0.1 M	~1.53	367	95	~0.40	49
	O–CoMoS	1.0 M	___	97	70	1	50
	CeO_x/$NiCo_2S_4$/CC	1.0 M	___	270	126	4.0	51
	FeSe/NC−PoFeSe	0.1 M	1.45	330	76	~0.20	52
	Fe–Co–P Hollow Sphere	1.0 M	___	252	33	0.2	53
	CeO_2-CoO	1.0 M		296	76.78	___	54
	CoMoNiS-NF-31	1.0 M	___	166	58.0	1.86	55
	$Co_3Fe/Ce_{0.025}$	1.0 M	___	285	47.25	0.362	56
	Ce_1−CoP	1.0 M	___	270	63.0	1.00	57

Table S15 Comparison of electrocatalytic HER performance of CO/R^0/RO with recently reported ECs in 1.0 M KOH solution.

	Materials	$\eta_{j=10\ mA\ cm^{-2}}$ (mV)	Tafel slope (mV dec^{-1})	Mass loading (mg cm^{-2})	References
	CO/R^0/CO	58	34.5	~0.11	This Work
Ru-based ECs	RuCoO$_x$	37	53.2	~0.396	28
	CoRu-O/A@HNC-2	85	72.5	___	31
	Ru/NBFNiSe$_2$/Mo$_2$CT$_x$	73	19.0	0.10	32
	RuCo-LNC-120	52	64.7	~0.5	44
	RuO$_2$/3DMNC	50.96	60.1	4.0	46
	a-RuTe$_2$ PNRs	36	36.0	0.2	47
	RuIrO$_x$	13	23.0	1.0	48
	s–RuS$_2$/S–rGO	25	29	0.464	58
	Ni@Ni$_2$P–Ru HNRs	31	41	0.286	59
	CoRu-MoS$_2$	52	55	___	60
Other Metal-based ECs	CoMoNiS-NF-31	113	85.0	1.86	55
	Co$_3$Fe/Ce$_{0.025}$	178	75.36	0.362	56
	Ce$_1$−CoP	144	70.0	1.00	57
	NiCo$_2$S$_4$/Ni$_3$S$_2$/NF	119	105.2	___	61
	MoS$_2$-Ni$_3$S$_2$Heteronanorod/NF	98	61	___	62
	Zn-Co-S/CFP	234	109	0.600	63
	MoSe$_2$@Ni$_{0.85}$Se/NF	117	66	6.480	64
	CoP/Co$_2$P/Co nanoparticles	175	84	0.200	65
	MoC@NCS-900	89	51	___	66
	AMO/PdO$_x$/Pd	58	37.8	0.160	10

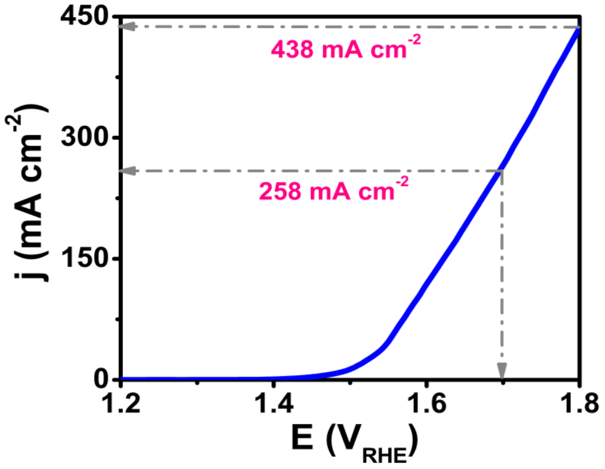

Fig. S41 LSV curves of CO/R^0/RO up to 438 mA.cm^{-2} current density during H_2O electrolysis.

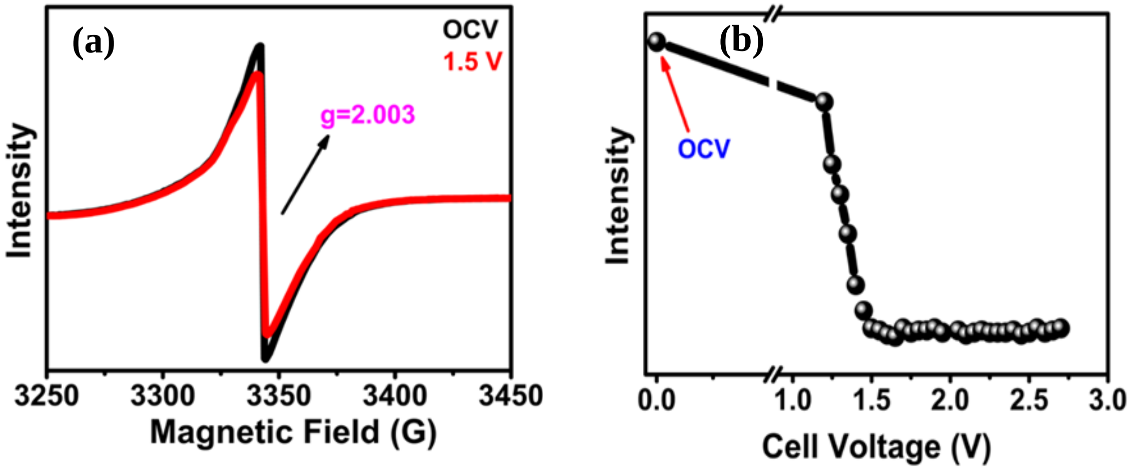

Fig. S42 (a) In-situ EPR and energetic activities for the HER and OER, (b) in-situ EPR spectra recorded at varied potentials.

Table S16 Comparison of electrocatalytic OER and ORR performances with recently reported bifunctional ECs.

	Materials	OER (1.0 M KOH)	ORR (0.1 M KOH)	$\Delta E = E_{j=10} - E_{1/2}$ (V_{RHE})	References
		$E_{j=10}$ (V_{RHE})	$E_{1/2}$ (V_{RHE})		
	CO/R^0/CO	1.34	0.936	0.414	This work
Ru-based ECs	Rh_6Cu_1/C	1.53	0.85	0.680	27
	$RuCoO_x$	1.505	0.855	0.650	28
	Ru/NBFNiSe_2/Mo_2CT_x	1.558	0.912	0.646	32
	$Ru_{0.1}$ZIS	1.506	0.845	0.660	67
	RuP/NPC	1.54	0.89	0.650	68
	Ru@NGA -900	1.62	0.700	0.920	69
Other Metal-based ECs	ppy/$AgVO_3$/porphy	1.45	0.89	0.56	13
	Co@IC/MoC@PC	1.512	0.875	0.637	34
	$(Co_9S_8$/N,S−DLCTs$)_{HF}$	1.597	0.890	0.707	49
	FeSe/NC−PoFeSe	1.56	0.86	0.7	52
	Cu-14-Co_3Se_4/GC	1.51	0.782	0.723	70
	CoP	1.56	0.858	0.702	71
	FeP_x/Fe–N–C/NPC	1.555	0.86	0.695	72
	FeS/Fe_3C@N-S-C-800	1.80	0.87	0.93	73
	NS/rGO-Co4	1.459	0.82	0.639	74
	Co_9S_8@MoS_2	1.572	0.884	0.688	75
	NCNT/CoFe-$CoFe_2O_4$	1.54	0.74	0.80	76
	CoS_x@Cu_2MoS_4-MoS_2/NSG	1.5814	0.89	0.6914	77
	Mo-N/C@MoS_2	1.62	0.81	0.81	78

Table S17 Comparison of performance of ZABs with other reported ECs in 6.0 M KOH solution.

	Materials	Current Density ($mA.cm^{-2}$)	Maximum power Density ($mW.cm^{-2}$)	References
	$CO/R^0/CO$	420.1	376.4	This work
Ru-based ECs	Rh_6Cu_1/C	___	142.58	27
	$RuCoO_x$	___	160	28
	$Ru/NBFNiSe_2/Mo_2CT_x$	___	192.3	32
	$R_{0.1}ZIS$	___	176.0	67
Other Metal-based ECs	$ppy/AgVO_3/porphy$	362	301	13
	CoP/C NWs	___	111.4	33
	$CoS_x@Cu_2MoS_4$- MoS_2/NSG	58	40	77
	$Mo\text{-}N/C@MoS_2$	250	200	78
	FeCo-N-C-700	240	150	79
	Co/N-PCC	180	127.86	80
	MnO@Co-N/C	225	130.3	81
	$Co\text{-}NC@Al_2O_3$	90	72.1	82
	Ni-Fe-MoN NTs	315	118	83
	$Co@Co_3O_4@NC\text{-}900$	60	64	84
	$Co_3O_4@Co/NCNT$	___	135	85
	S,N-co-doped bamboo carbons (SNBC-12)	___	156	86
	Pt-SCFP/C-12	214	122	87

Table S18 Performance comparison of CO/R^0/RO with recently reported trifunctional ECs.

	Materials	Electrolyte (KOH)	$\eta_{j=10\ \mathrm{mA\ cm^{-2}}}$ (mV$_{\mathrm{RHE}}$)		$E_{1/2}$ (V$_{\mathrm{RHE}}$)	Tafel slope (mV dec^{-1})			References
			HER	OER	ORR	HER	OER	ORR	
	CO/R^0/CO	1.0 M	58	120		34.5	61.3		This work
		0.1 M			0.936			53.2	
Ru-based ECs	Rh_6Cu_1/C	1.0 M	36	300		35	70		27
		0.1 M			0.85			55	
	$RuCoO_x$	1.0 M	37	275		53.2	54		28
		0.1 M			0.855			46.7	
	$Ru/NBFNiSe_2/Mo_2CT_x$	1.0 M	39	328		29			32
		0.1 M			0.912				
Other Metal-based ECs	CoP	1.0 M	62.5	330		69.2	89.7		71
		0.1 M			0.858			72.1	
	Cu-14-Co_3Se_4/GC	1.0 M	166	280		168	111		88
		0.1 M			0.782			56	
	FeP_x/Fe-N-C/NPC	1.0 M	182	325		132	79		89
		0.1 M			0.86			—	
	FeS/Fe_3C@N-S-C-800	1.0 M	450	570		95	81		90
		0.1 M			0.87			90	
	PPy/FeTCPP/Co	1.0 M	270	340		84	65		91
		0.1 M			0.86			69	
	am-Fe–Bi/NF	1.0 M	143	158		75	53		92
		0.1 M			0.8				
	NCNT/CoFe-$CoFe_2O_4$	1.0 M	204	310		91	63		93
		0.1 M			0.74				
	Co_9S_8@MoS_2	1.0 M	143	342		117	94		94
		0.1 M			0.884				

Table S19 Performance comparison of CO/R^0/RO with recently reported bifunctional ECs for two-electrode overall water splitting in 1.0 M KOH solution.

	Materials	Catalyst Support	Mass loading (mg cm^{-2})	$E_{10\ mA\ cm^{-2}}$ (V_{RHE})	References
	CO/R^0/CO ‖ CO/R^0/CO	Ni foam	0.10	1.49	This work
Ru-based ECs	Rh_6Cu_1/C‖ Rh_6Cu_1/C	Carbon cloth	1.0	1.55	27
	$RuCoO_x$ ‖ $RuCoO_x$	Carbon cloth	1.0	1.54	28
	CoRu-O/A@HNC-2 ‖ CoRu-O/A@HNC-2	Carbon cloth	___	1.558	31
	SiO_x/Ru‖ SiO_x/Ru	Ni foam	0.25	1.496	43
	Ru/NF-2 ‖ Ru/NF-2	Ni foam	0.05	1.56	45
	$RuIrO_x$‖ $RuIrO_x$	Carbon fiber paper	1.0	1.47	48
	s–RuS_2/S–rGO ‖ RuO_2/C	Ni foam	5.0	1.52	58
	RuCo-NC-120 ‖ RuCo-NC-120	Carbon cloth	~0.5	1.531	95
	Ru/3DMNC ‖ RuO_2/3DMNC	Ni foam	4.0	1.51	96
Other Metal-based ECs	AMO/PdO_x/Pd ‖ AMO/PdO_x/Pd	Ni foam	0.25	1.50	10
	$Co_3Fe/Ce_{0.025}$ ‖ $Co_3Fe/Ce_{0.025}$	Carbon paper	1.0	1.70	56
	NCS ‖ MoC@NCS	Ni foam	1.0	1.69	66
	Ce_1-CoP ‖ Ce_1-CoP	Graphite paper	1.0	1.65	97
	NiS ‖ NiS	Ni foam	1.2	1.61	98
	CoMoNiS-NF-31 ‖ CoMoNiS-NF-31	Ni foam	1.86	1.54	99
	CoP/NCNHP‖ CoP/NCNHP	Carbon paper	2.0	1.64	100

Controlled-Potential Electrolysis (CPE)

Table S20 Controlled potential electrolysis for CO/R^0/RO.

ECs	Electrolysis Time (Sec)	Charge (C)	Gas Evolved (mL)	Faradic Efficiency (%)
CO/R^0/RO	60000	197	16.8	98.2

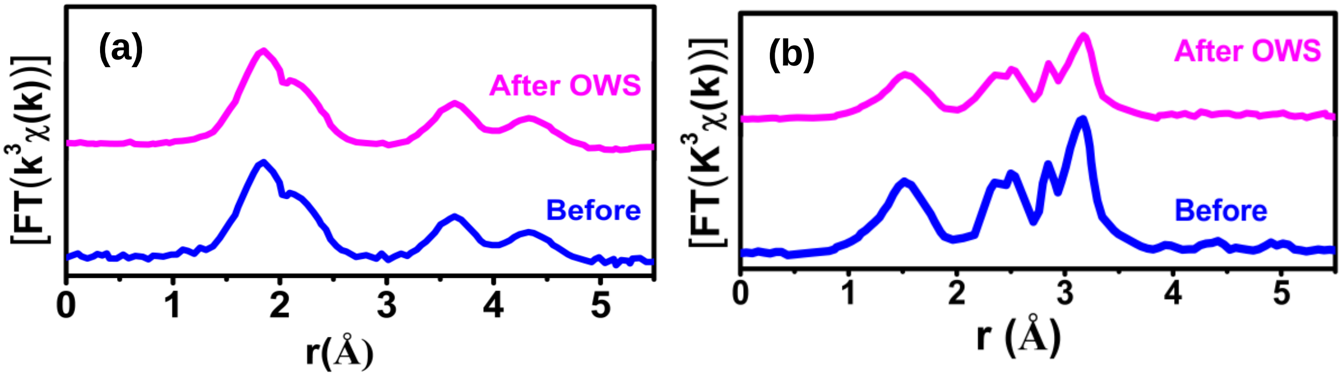

Fig. S43 Fourier transform (FT) (a) Ce K-edge, and (b) Ru K-edge k^3-weighted EXAFS spectra of CO/R^0/R before and after OWS.

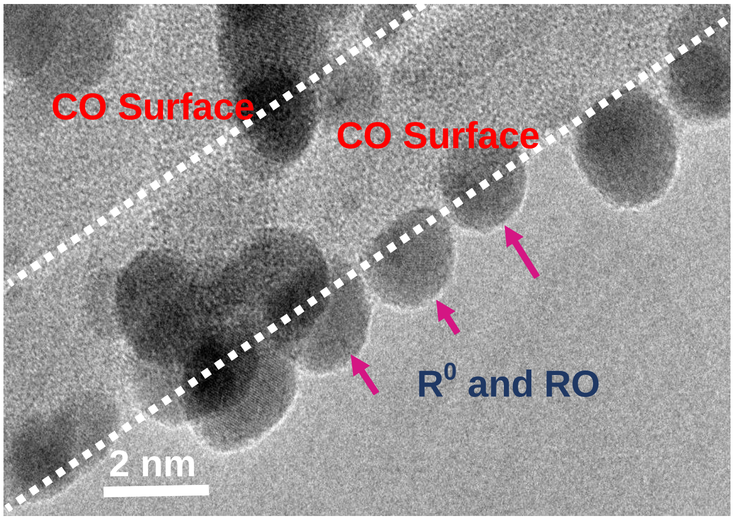

Fig. S44 TEM image of CO/R^0/RO after OWS.

S10. Purification of alkaline electrolyte

In commercial KOH solution, some impurities are usually present in the form of trace amounts of transition metals (T_Ms) which may possibly affect the catalytic performances of the EC due to probable contamination of catalyst surface by the 3d-T_M hydr(oxy)oxides. During ORR/OER/HER, the 3d-T_M impurities probably block the active sites of EC for intermediate adsorption and subsequently a noticeable decrease of its activity may expect. While in purified KOH, the active sites are remained free from contamination of T_M impurities. In contrast, T_M hydr(oxy)oxides are very active for OER. Thus, ECs sometimes display anomalous behavior in commercial KOH solution. From inductively coupled plasma mass spectroscopy (ICPMS), Fe is observed to present in ~ 0.1 ppm level among the common impurities (Fe, Co, Ni, Cu, Cr) that may affect catalytic activity of the ECs. Therefore, we have purified the commercial KOH[8,11] solution and used this purified KOH in our entire experiments.

In order to remove trace Fe, high purity $Ni(OH)_2$ precipitate is used as an Fe absorbent. Initially, $Ni(NO_3)_2 \cdot 6H_2O$ is dissolved in H_2O in polypropylene tube. After that, 1.0 M NaOH is put into dropwise the above solution to get high-purity $Ni(OH)_2$ precipitate. The mixture is kept for ultrasonication for 30min, and then centrifuged. Finally, the $Ni(OH)_2$ is collected followed by repetitive washing with H_2O and 1.0 M NaOH. Subsequently, 0.1/1.0 M KOH is poured into the tube for purification. Ultrasonic vibration is continued further for redispersion of the solid and then mechanically agitated for 30min, followed by at least 4h of resting. Lastly, the purified KOH supernatant is collected through centrifugation and put into a polypropylene bottle for storage to use during whole electrochemical experiments.

Table S21 ICPMS result for commercial KOH solution.

	Ion contents (μg/L)				
Commercial KOH	Fe	Co	Ni	Cu	Cr
	~ 102	~ 5	~ 5	~ 2	~3

Table S22 ICPMS result for purified KOH solution.

	Ion contents (μg/L)				
Purified KOH	Fe	Co	Ni	Cu	Cr
	~ 2	~ 5	~5	~ 2	~ 3

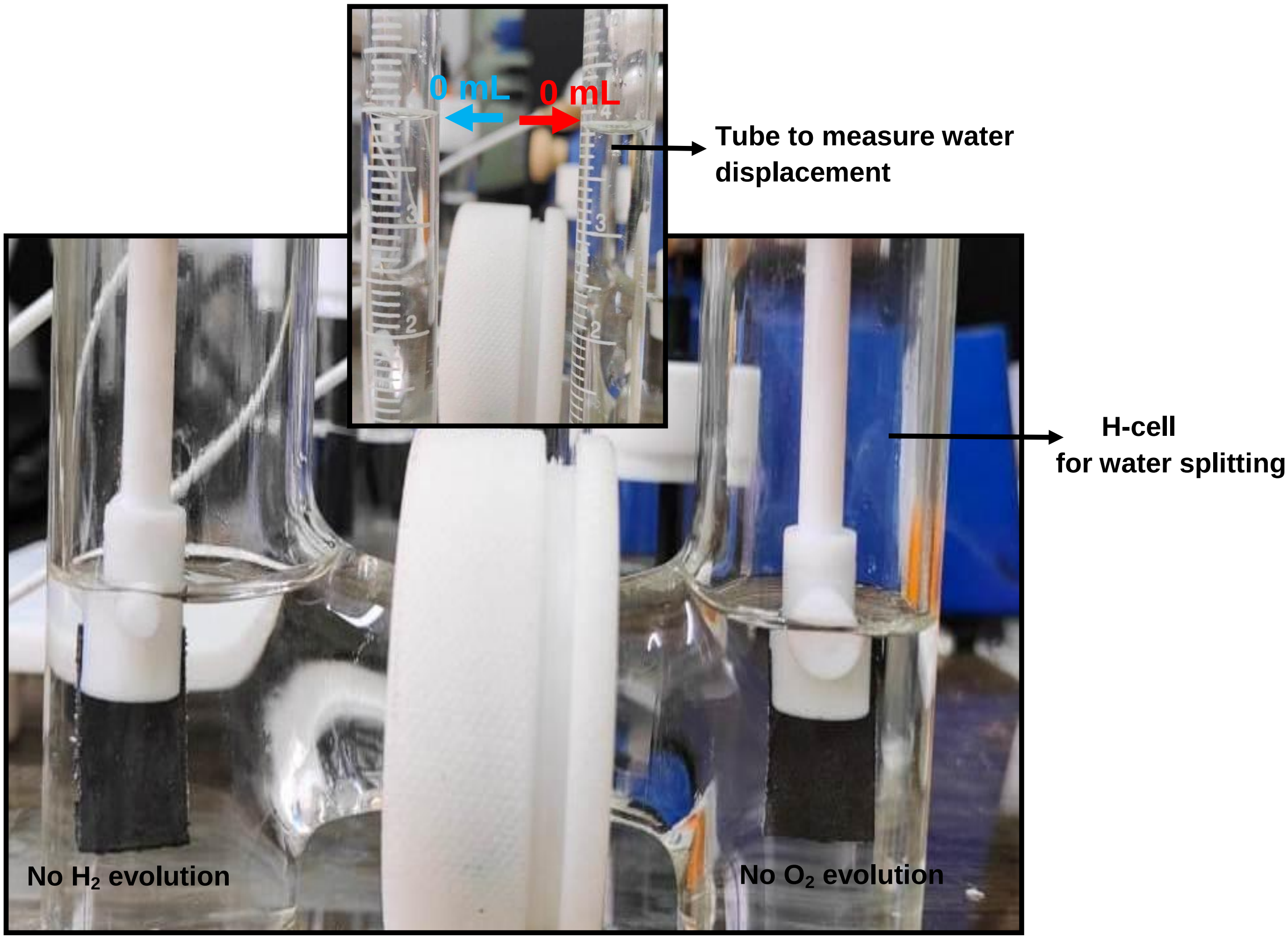

Fig. S45 Optical image showing the electrochemical water splitting setup (before connection to the ZAB i.e., circuit is turned off).

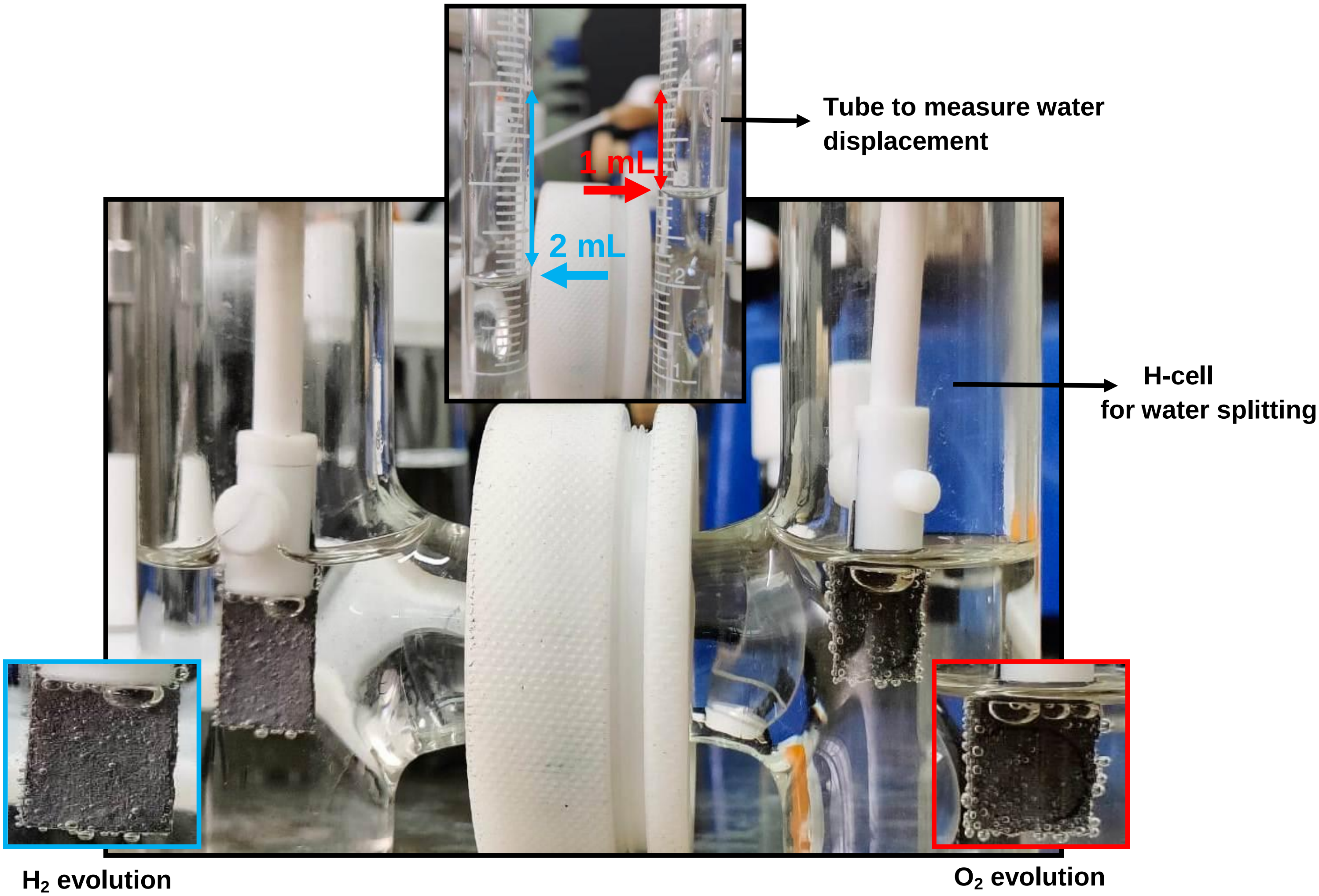

Fig. S46 Optical image showing the electrochemical water splitting setup (after connection to the ZAB i.e., circuit is turned on).

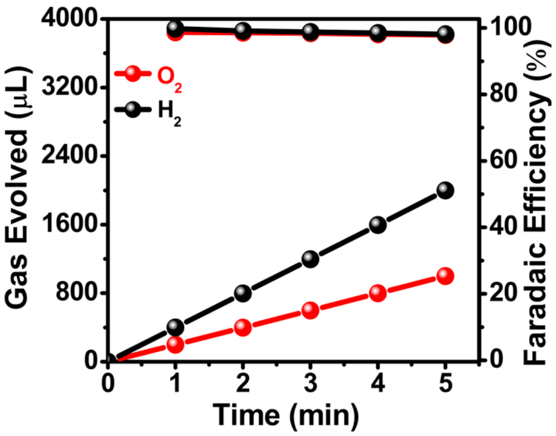

Fig. S47 Rate and Faradaic efficiency of H_2 and O_2 evolution.

S11. Determination of the Faradaic Efficiency (FE %)

The FE% of water splitting catalyzed by CO/R^0/RO was calculated by comparing the experimentally produced gas volume with the theoretically calculated one:

$$\mathrm{FE\%} = V_{\mathrm{experimental}} / V_{\mathrm{theoretical}} \qquad \textbf{(S30)}$$

The experimental volumes of H_2 and O_2 were measured by drainage method. The theoretical volume can be calculated by using the formula $V_{\mathrm{theoretical}} = C_{\mathrm{Zn}} \cdot M_{\mathrm{Zn}} \cdot V_m / n \cdot F$ where C_{Zn} is the theoretical specific capacity of zinc (2952 C/g), M_{Zn} is the quantity of zinc loss, V_m is the molar volume of H_2 or O_2 in 1 mol (24.1 L/mol, 298 K, 101 kPa), n is the number of electrons needed for 1 mol of H_2 or O_2, and F is the Faradaic constant (96,485 C/mol).

$$\mathrm{FE}_{\mathrm{H2}} = V_{\mathrm{experimental}} / V_{\mathrm{theoretical}} = V_{\mathrm{experimental}} / [(2/4) \times \{(C_{\mathrm{Zn}} \times M_{\mathrm{Zn}})/F\} \times V_m] \qquad \textbf{(S31)}$$

$$\mathrm{FE}_{\mathrm{O2}} = V_{\mathrm{experimental}} / V_{\mathrm{theoretical}} = V_{\mathrm{experimental}} / [(1/4) \times \{(C_{\mathrm{Zn}} \times M_{\mathrm{Zn}})/F\} \times V_m] \qquad \textbf{(S32)}$$

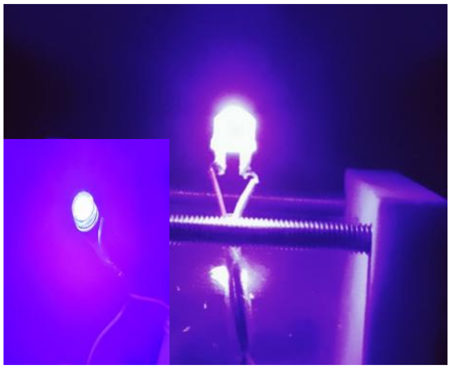

Fig. S48 Photograph of a LED light lit by CO/R^0/RO-based ZAB.

References

1 X. Wu, W. Qian, H. Zhang, Z. Han, H. Zhang, H. Ma, D. Liu, Q. Sun and W. Ying, *Catal. Sci. Technol.*, 2021, **11**, 2577-2588.

2 Z. Hu, X. Liu, D. Meng, Y. Guo, Y. Guo and G. Lu, *ACS Catal.*, 2016, **6**, 2265-2279.

3 T. Wang, Z. Li, H. Jang, M. G. Kim, Q. Qin and X. Liu, *ACS Sustainable Chem. Eng.*, 2023, **11**, 5155-5163.

4 S. Gupta, M. Sinha, R. Dhawan, R. Jangir, A. Bose, P. Gupta, M. K. Swami and M. H. Modi, *Thin Solid Films* 2023, **764**, 139606 (1-7).

5 B. Ravel and M. Newville, *J. Synchrotron Rad.*, 2005, **12**, 537-541.

6 M. Newville, *J. Synchrotron Rad.*, 2001, **8**, 96-100.

7 P. He, T. Zhang, J. Jiang and H. Zhou, *J. Phys. Chem. Lett.*, 2016, **7**, 1267-1280.

8 Z. Chang, X. Wang, Y. Yang, J. Gao, M. Li, L. Liu and Y. Wu, *J. Mater. Chem. A* 2014, **2**, 19444-19450.

9 Z. Chang, F. Yu, Z. Liu, S. Peng, M. Guan, X. Shen, S. Zhao, N. Liu, Y. Wu and Y. Chen, *ACS Appl. Mater. Interfaces* 2020, **12**, 4366-4372.

10 P. Mondal, J. Satra, D. N. Srivastava, G. R. Bhadu and B. Adhikary, *ACS Catal*., 2021, **11**, 3687-3703.

11 M. Kölbacha, S. Fiechtera, R. v. d. Krola and P. Bogdanoffa, *Catal*., 2017, **290**, 2-9.

12 C. C. L. McCrory, S. Jung, J. C. Peters and T. F. Jaramillo, *J. Am. Chem. Soc*., 2013, **135**, 16977-16987.

13 P. Mondal, U. K. Ghorui, J. Satra, S. Mardanya, D. N. Srivastava, G. R. Bhadu and B. Adhikary, *ACS Appl. Nano Mater*., 2020, **3**, 3876-3891.

14 C. C. L. McCrory, S. Jung, I. M. Ferrer, S. M. Chatman, J. C. Peters and T. F. Jaramillo, *J. Am. Chem. Soc*., 2015, **137**, 4347-4357.

15 P. Connor, J. Schuch, B. Kaiser and W. *Z.* Jaegermann, *Phys. Chem*., 2020, **5**, 979-994.

16 S. Niu, W. J. Jiang, Z. Wei, T. Tang, J. Ma, J. S. Hu and L. J. Wan, *J. Am. Chem. Soc*., 2019, **141**, 7005-7013.

17 X. Liu, S. Cui, Z. Sun, Y. Ren, X. Zhang and P. Du, *J. Phys. Chem. C* 2016, **2**, 831-840.

18 Zhang, T.; J. Du, P. Xi and C. Xu, *ACS Appl. Mater. Interfaces* 2017, **9**, 362-370.

19 J. Yang, G. Zhu, Y. Liu, J. Xia, Z. Ji, X. Shen and S. Wu, *Adv. Funct. Mater.*, 2016, **26**, 4712-4721.

20 Z. Q. Liu, H. Cheng, N. Li, T. Y. Ma and Y. Z. Su, *Adv. Mater.*, 2016, **28**, 3777-3784.

21 V. Maruthapandian, M. Mathankumar, V. Saraswathy, B. Subramanian and S. Muralidharan, *ACS Appl. Mater. Interfaces* 2017, **9**, 13132-13141.

22 L. Li, H. Yang, J. Miao, L. Zhang, H. Y. Wang, Z. Zeng, W. Huang, X. Dong and B. Liu, *ACS Energy Lett.*, 2017, **2**, 294-300.

23 J. Zhang, X. Bai, T. Wang, W. Xiao, P. Xi, J. Wang, D. Gao and J. Wang, *Nanomicro Lett.*, 2019, **11**, 2-13.

24 Z. F. Huang, J. Wang, Y. Peng, C. Y. Jung, A. Fisher and X. Wang, *Adv. Energy Mater.*, 2017, **7**, 1700544(1-21).

25 D. Das, S. Santra and K. K. Nanda, *ACS Appl. Mater. Interfaces* 2018, **10**, 35025-35038.

26 Y. Dang, T. Wu, H. Tan, J. Wang, C. Cui, P. Kerns, W. Zhao, L. Posada, L. Wen and S. L. Suib, *Energy Environ. Sci.*, 2021, **14**, 5433-5443.

27 W. Zhang, J. Zhao, J. Zhang, X. Chen, X. Zhang and F. Yang, *ACS Appl. Mater. Interfaces* 2020, **12**, 10299-10306.

28 C. Zhou, S. Zhao, H. Meng, Y. Han, Q. Jiang, B. Wang, X. Shi, W. Zhang, L. Zhang and R. Zhang, *Nano Lett.*, 2021, **21**, 9633-9641.

29 M. Retuerto, F. Calle-Vallejo, L. Pascual, G. Lumbeeck, M. T. Fernandez-Diaz, M. Croft, J. Gopalakrishnan, M. A. Peña, J. Hadermann, M. Greenblatt and S. Rojas, *ACS Appl. Mater. Interfaces* 2019, **11**, 21454-21464.

30 N. Kumar, K. Naveen, M. Kumar, T. C. Nagaiah, R. Sakla, A. Ghosh, V. Siruguri, S. Sadhukhan, S. Kanungo and A. K. Paul, *ACS Appl. Energy Mater.*, 2021, **4**, 1323-1334.

31 G. Li, K. Zheng, W. Li, Y. He and C. Xu, *ACS Appl. Mater. Interfaces* 2020, **12**, 51437-51447.

32 M. Yi, X. Zhang, Y. Chen, H. Wan, L. Xie, X. Huang, Z. Zhu and J. Zhang, *ACS Sustainable Chem. Eng.*, 2023, **11**, 3687-3701.

33 K. Tang, L. Chen, Y. Xiong, L. Zhang and M. Wu, *ACS Appl. Nano Mater.*, 2023, **6**, 11553-11560.

34 L. Zhang, Y. Zhu, Z. Nie, Z. Li, Y. Ye, L. Li, J. Hong, Z. Bi, Y. Zhou and G. Hu, *ACS Nano* 2021, **15**, 13399-13414.

35 Q. Xiang, Y. Liu, X. Zou, B. Hu, Y. Qiang, D. Yu, W. Yin and C. Chen, *ACS Appl. Mater. Interfaces* 2018, **10**, 10842-10850.

36 L. Liu, Q. Wei, X. Yu and Y. Zhang, *ACS Appl. Mater. Interfaces* 2018, **10**, 34068-34076.

37 L. Zhao, Q. Wang, X. Zhang, C. Deng, Z. Li, Y. Lei and M. Zhu, *ACS Appl. Mater. Interfaces* 2018, **10**, 35888-35895.

38 K. Maiti, J. Balamurugan, J. Gautam, N. H. Kim and J-H. Lee, *ACS Appl. Mater. Interfaces* 2018, **10**, 32220-32232.

39 T. D. Thanh, N. D. Chuong, H. V. Hien, N. H. Kim and J. H. Lee, *ACS Appl. Mater. Interfaces* 2018, **10**, 4672-4681.

40 D. Ji, L. Fan, L. Tao, Y. Sun, M. Li, G. Yang, T. Q. Tran, S. Ramakrishna and S. Guo, *Angew. Chem. Int. Ed*., 2019, **58**, 13840.

41 K. Maiti, J. Balamurugan, S. G. Peera, N. H. Kim and J. H. Lee, *ACS Appl. Mater. Interfaces* 2018, **10**, 18734-18745.

42 N. D. Chuong, T. D. Thanh, N. H. Kim and J. H. Lee, *ACS Appl. Mater. Interfaces* 2018, **10**, 24523-24532.

43 T. Zhu, J. Han, T. Sun, J. Chen, S. Wang, S. Ren, X. Pi, J. Xu and K. Chen, *ACS Appl. Mater. Interfaces* 2023, **15**, 8200-8207.

44 H. Li, W. Ma, X. Ma, M. Guo and G. Li, *ACS Sustainable Chem. Eng*., 2022, **10**, 16214-16224.

45 Y. Pei, S. Guo, Q. Ju, Z. Li, P. Zhuang, R. Ma, Y. Hu, Y. Zhu, M. Yang, Y. Zhou, J. Shen and J. Wang, *ACS Appl. Mater. Interfaces* 2020, **12**, 36177-36185.

46 D. Li, X. Shi, S. Sun, X. Zheng, D. Tian and D. Jiang, *Inorg. Chem.*, 2022, **61**, 9685-9692.

47 J. Wang, L. Han, B. Huang, Q. Shao, H. L. Xin and X. Huang, *Nat. Commun*., 2019, **10**, 5692.

48 Z. Zhuang, Y. Wang, C. Q. Xu, S. Liu, C. Chen, Q. Peng, Z. Zhuang, H. Xiao, Y. Pan, S. Lu, R. Yu, W. C. Cheong, X. Cao, K. Wu, K. Sun, Y. Wang, D. Wang, J. Li and Y. Li, *Nat. Commun*., 2019, **10**, 4875.

49 C. Hu, J. Liu, J. Wang, W. She, J. Xiao, J. Xi, Z. W. Baia and S. Wang, *ACS Appl. Mater. Interfaces* 2018, **10**, 33124-33134.

50 J. Hou, B. Zhang, Z. Li, S. Cao, Y. Sun, Y. Wu, Z. Gao and L. Sun, *ACS Catal*., 2018, **8**, 4612-4621.

51 X. Wu, Y. Yang, T. Zhang, B. Wang, H. Xu, X. Yan and Y. Tang, *ACS Appl. Mater. Interfaces* 2019, **11**, 39841-39847.

52 G. Wang, J. Li, M. Liu, L. Du and S. Liao, *ACS Appl. Mater. Interfaces* 2018, **10**, 32133-32141.

53 K. Liu, C. Zhang, Y. Sun, G. Zhang, X. Shen, F. Zou, H. Zhang, Z. Wu, E. C. Wegener, C. J. Taubert, J. T. Miller, Z. Peng and Y. Zhu, *ACS Nano* 2018, **12**, 158-167.

54 W. Li, L. Zhao, C. Wang, X. Lu and W. Chen, *ACS Appl. Mater. Interfaces* 2021, **13**, 46998-47009.

55 Y. Yang, H. Yao, Z. Yu, S. M. Islam, H. He, M. Yuan, Y. Yue, K. Xu, W. Hao, G. Sun, H. Li, S. Ma, P. Zapol and M. G. Kanatzidis, *J. Am. Chem. Soc*., 2019, **141**, 10417-10430.

56 X. Z. Song, T. Zhang, Y. H. Zhao, J. C. Ni, Y. Pan, Z. Tan and X. F. Wang, *Inorg. Chem*., 2023, **62**, 8347-8356.

57 J. Li, S. Zou, X. Liu, Y. Lu and D. Dong, *ACS Sustainable Chem. Eng*., 2020, **8**, 10009-10016.

58 J. Yu, Y. Guo, S. Miao, M. Ni, W. Zhou and Z. Shao, *ACS Appl. Mater. Interfaces* 2018, **10**, 34098-34107.

59 Y. Liu, S. Liu, Y. Wang, Q. Zhang, L. Gu, S. Zhao, D. Xu, Y. Li, J. Bao and Z. Dai, *J. Am. Chem. Soc*., 2018, **140**, 2731-2734.

60 I. S. Kwon, T. T. Debela, I. H. Kwak, Y. C. Park, J. Seo, J. Y. Shim, S. J. Yoo, J.-G. Kim, J. Park and H. S. Kang, *Small* 2020, **16**, e2000081.

61 H. Liu, X. Ma, Y. Rao, Y. Liu, J. Liu, L. Wang and M. Wu, *ACS Appl. Mater. Interfaces* 2018, **10**, 10890-10897.

62 Y. Q. Yang, K. Zhang, H. L. Lin, X. Li, H. C. Chan, L. C. Yang and Q. S. Gao, *ACS Catal*., 2017, **7**, 2357-2366.

63 X. Y. Xu, X. P. Han, X. Y. Ma, W. Zhang, Y. D. Deng, C. Zhong and W. B. Hu, *ACS Appl. Mater. Interfaces* 2017, **9**, 12574-12583.

64 C. Q. Wang, P. Zhang, J. L. Lei, W. Dong and J. H. Wang, *Electrochim. Acta* 2017, **246**, 712-719.

65 A. Sumboja, T. An, H. Y. Goh, M. Lübke, D. P. Howard, Y. Xu, A. D. Handoko, Y. Zong and Z. Liu, *ACS Appl. Mater. Interfaces* 2018, **10**, 15673-15680.

66 J. T. Ren, L. Chen, C. C. Weng, G. G. Yuan and Z. Y. Yuan, *ACS Appl. Mater. Interfaces* 2018, **10**, 33276-33286.

67 Z. Hou, Z Sun, C. Cui, D. Zhu, Y. Yang and T. Zhang, *Adv. Funct. Mater*., 2022, **32**, 2110572.

68 Q. Qin, H. Jang, L. Chen, G. Nam, X. Liu and J. Cho, *Adv. Energy Mater*., 2018, **8**, 1801478.

69 B. Zhu, C. Qu, S. Gao, Z. liang, H. Zhang and P. R. Zou, *ChemCatChem* 2018, **10**, 1113-1121.

70 J. L. Dai, D. K. Zhao, W. M. Sun, X. J. Zhu, L.-J. Ma, Z. X. Wu, C. H. Yang, Z. M. Cui, L. G. Li and S. W. Chen, *ACS Catal*., 2019, **9**, 10761-10772.

71 H. Li, Q. Li, P. Wen, T. B. Williams, S. Adhikari, C. C. Dun, C. Lu, D. Itanze, L. Jiang, D. L. Carroll, G. L. Donati, P. M. Lundin, Y. J. Qiu and S. M. Geyer, *Adv. Mater*., 2018, **30**, 1705796.

72 Q. Qin, H. Jang, P. Li, B. Yuan, X. E. Liu and J. Cho, *Adv. Energy Mater*., 2018, **9**, 1803312.

73 F. T. Kong, X. H. Fan, A. G. Kong, Z. Q. Zhou, X. Y. Zhang and Y. K. Shan, *Adv. Funct. Mater*., 2018, **28**, 1803973.

74 N. Wang, L. G. Li, D. K. Zhao, X. W. Kang, Z. H. Tang and S. W. Chen, *Small* 2017, **13**, 1701025.

75 J. M. Bai, T. Meng, D. L. Guo, S. G. Wang, B. G. Mao and M. H. Cao, *ACS Appl. Mater. Interfaces* 2018, **10**, 1678-1689.

76 Q. Qin, P. Li, L. L. Chen and X. E. Liu, *ACS Appl. Mater. Interfaces* 2018, **10**, 39828-39838.

77 D. C. Nguyen, D. T. Tran, T. L. L. Doan, D. H. Kim, N. H. Kim and J. H. Lee, *Adv. Energy Mater*., 2020, **8**, 1903289.

78 B. Ouyang, N. Artrith, Z. Y. Lun, Z. Jadidi, D. A. Kitchaev, H. W. Ji, A. Urban and G. Ceder, *Adv. Energy Mater*., 2020, **10**, 1903240.

79 X. D. Duan, S. S. Ren, N. Pan, M. D. Zhang and H. G. Zheng, *J. Mater. Chem. A* 2020, **8**, 9355-9363.

80 Q. X. Luo, L. P. Guo, S. Y. Yao, J. Bao, Z. T. Liu and Z. W. Liu, *J Catal*., 2019, **369**, 143-156.

81 Y. N. Chen, Y. B. Guo, H. J. Cui, Z. J. Xie, X. Zhang, J. P. Wei and Z. Zhou, *J. Mater. Chem. A* 2018, **6**, 9716-9722.

82 L. Zhu, D. Z. Zheng, Z. F. Wang, X. S. Zheng, P. P. Fang, J. F. Zhu, M. H. Yu, Y. X. Tong and X. H. Lu, *Adv. Mater*., 2018, **30**, 1805268.

83 C. L. Zhu, Z. X. Yin, W. H. Lai, Y. Sun, L. N. Liu, X. T. Zhang, Y. J. Chen and S. L. Chou, *Adv. Energy Mater*., 2018, **8**, 1802327.

84 Z. Y. Guo, F. M. Wang, Y. Xia, J. L. Li, A. G. Tamirat, Y. R. Liu, L. Wang, Y. G. Wang and Y. Y. Xia, *J. Mater. Chem. A* 2018, **6**, 1443-1453.

85 T. Singh, C. Das, N. Bothra, N. Sikdar, S. Das, S. K. Pati and T. K. Maji, *Inorg. Chem*., 2020, **59**, 3160-3170.

86 M.-J. Kim, J. E. Park, S. Kim, M. S. Lim, A. Jin, O.-H. Kim, M. J. Kim, K.-S. Lee, J. Kim, S.-S. Kim, Y.-H. Cho and Y.-E. Sung, *ACS Catal*., 2019, **9**, 3389-3398.

87 X. Wang, J. Sunarso, Q. Lu, Z. Zhou, J. Dai, D. Guan, W. Zhou and Z. Shao, *Adv. Energy Mater*., 2019, **10**, 1903271.

88 J. L. Dai, D. K. Zhao, W. M. Sun, X. J. Zhu, L.-J. Ma, Z. X. Wu, C. H. Yang, Z. M. Cui, L. G. Li and S. W. Chen, *ACS Catal*., 2019, **9**, 10761-10772.

89 Q. Qin, H. Jang, P. Li, B. Yuan, X. Liu and J. Cho, *Adv. Energy Mater*., 2018, **9**, 1803312.

90 F. T. Kong, X. H. Fan, A. G. Kong, Z. Q. Zhou, X. Y. Zhang and Y. K. Shan, *Adv. Funct. Mater*., 2018, **28**, 1803973.

91 J. Yang, X. Wang, B. Li, L. Ma, L. Shi, Y. J. Xiong and H. X. Xu, *Adv. Funct. Mater*., 2017, **27**, 1606497.

92 W. N. Zhao, T. Xu, T. Li, Y. K. Wang, H. Liu, J. Z. Feng, S. J. Ding, Z. T. Li and M. B. Wu, *Small* 2018, **14**, 1802829.

93 Q. Qin, P. Li, L. L. Chen and X. E. Liu, *ACS Appl. Mater. Interfaces* 2018, **10**, 39828-39838.

94 J. M. Bai, T. Meng, D. L. Guo, S. G. Wang, B. G. Mao and M. H. Cao, *ACS Appl. Mater. Interfaces* 2018, **10**, 1678-1689.

95 H. Li, W. Ma, X. Ma, M. Guo and G. Li, *ACS Sustainable Chem. Eng*., 2022, **10**, 16214-16224.

96 D. Li, X. Shi, S. Sun, X. Zheng, D. Tian and D. Jiang, *Inorg. Chem.*, 2022, **61**, 9685-9692.

97 J. Li, S. Zou, X. Liu, Y. Lu and D. Dong, *ACS Sustainable Chem. Eng.*, 2020, **8**, 10009-10016.

98 J. T. Ren and Z. Y. Yuan, *ACS Sustainable Chem. Eng.*, 2017, **5**, 7203-7210.

99 Y. Yang, H. Yao, Z. Yu, S. M. Islam, H. He, M. Yuan, Y. Yue, K. Xu, W. Hao, G. Sun, H. Li, S. Ma, P. Zapol and M. G. Kanatzidis, *J. Am. Chem. Soc.*, 2019, **141**, 10417-10430.

100 Y. Pan, K. Sun, S. Liu, X. Cao, K. Wu, W. C. Cheong, Z. Chen, Y. Wang, Y. Li, Y. Liu, D. Wang, Q. Peng, C. Chen and Y. Li, *J. Am. Chem. Soc.*, 2018, **140**, 2610-2618.